PHYSICAL REVIEW B **100**, 134301 (2019)

Dynamical synchronization transition in interacting electron systems

Tanay Nag[1], Robert-Jan Slager[1], Takuya Higuchi[2] and Takashi Oka[1,3]
[1]*Max Planck Institute for the Physics of Complex Systems, Dresden 01187, Germany*
[2]*Chair of Laser Physics, Department of Physics, Friedrich-Alexander-Universität Erlangen-Nürnberg (FAU), Staudtstr. 1, D-91058 Erlangen, Germany*
[3]*Max Planck Institute for Chemical Physics of Solids, Dresden 01187, Germany*

(Received 22 January 2019; revised manuscript received 17 July 2019; published 1 October 2019)

Synchronization is a ubiquitous phenomenon in nature and we propose its new perspective in ultrafast dynamics in interacting electron systems. In particular, using graphene irradiated by an intense bicircular pulse laser as a prototypical and experimental viable example, we theoretically investigate how to selectively generate a coherent oscillation of electronic order such as charge density orders (CDOs). The key is to use tailored fields that match the crystalline symmetry broken by the target order. After the pump, a macroscopic number of electrons start oscillating and coherence is built up through a transition. The resulting physics is detectable as a coherent light emission at the synchronizion frequency and may be used as a purely electronic way of realizing Floquet states respecting exotic space-time crystalline symmetries. In the process, we also explore possible flipping of existing static CDOs and generation of higher harmonics. The general framework for the coherent electronic order is found to be analogous with the celebrated Kuramoto model, describing the classical synchronization of coupled pendulums.

DOI: 10.1103/PhysRevB.100.134301

I. INTRODUCTION

Control of quantum matter using nonequilibrium means is an important topic in fundamental science. In ultrafast pump-probe spectroscopy, well-controlled intense lasers are used to induce nonequilibrium phase transitions (reviewed in Refs. [1–5]) and one of the initial ideas was to use the laser-excited carriers to trigger a photoinduced insulator-to-metal transition in strongly correlated materials [6–8]. In this way, it is able to *destroy* orders present in the materials. However, *creating* a nontrivial order is not straightforward. One route is to resonantly pump coherent phonon oscillations optimizing the lattice structure to favor interesting electronic orders [9–12]. Quench-induced topological phases would also fall in this category [13,14]. Another route is Floquet engineering [15–17], a control of quantum states by periodic driving, and nontrivial topological states have been proposed [18–22] and realized [23–25]. Here, we study a hybrid of these two ideas. Namely, we study how to generate coherent electron oscillations in interacting electron systems with an aim to realize novel Floquet states. To be more specific, we investigate orders oscillating with a frequency Ω_0:

$$\langle c_a^\dagger(t)c_b(t)\rangle = \Delta_{ab}e^{-i(\Omega_0 t-\phi)} + \cdots \tag{1}$$

that did not exist in the ground state but are created by a short and intense pump laser field. Here, a, b denote the position (and spin, orbital ...) indices and the amplitude Δ_{ab} is at most a slowly changing function. Various oscillations of density order [charge density order (CDO), spin density order, bond density order, etc.] fit into this category. Most prominent examples are condensation of exciton and polariton, where coherently oscillating order parameters are realized [26,27]. We note that a dynamical order "Floquet condensation" analogous to (1) was also found in strongly interacting gauge theories, but the microscopic understanding of the mechanism is still lacking [28].

On the other hand, the discovery of the quantized Hall effects [29,30] has paved the way for a new class of topological quantum phenomena. In these instances, the defining properties are robust against perturbations that do not close the energy gap of the bulk excitation spectrum and are exhibited through the nontrivial topological structure of the ground-state wave function of the system [31]. More recently, these ideas reinvigorated due to the possibility of an interplay between both paradigms, as it was found that topological structures can appear due to the presence of symmetry. In this direction, a plethora of theoretical and experimental studies are devoted to understand the physics of topological insulators [32,33]. Similarly, gapless and semimetallic Dirac materials exhibit many unconventional properties such as a quantum Hall effect at room temperature [34] and a chiral-anomaly-induced negative magnetoresistance [35]. Topological phenomena are nevertheless not privileged to static systems. Microwave and optical techniques are increasingly being employed to realize topological band structures out of trivial materials [18,19,36–41]. Additionally, topological phenomena have been observed in dissipative quantum systems [42,43] and photonic experiments [25,44]. Lastly, light-irradiated graphene in many other aspects has been a prime field of theoretical and experimental research [45–49].

In our work, we show that a desired coherent oscillation can be selectively created by using pump fields that are carefully tailored. This is in contrast to the Higgs amplitude mode [50–56], i.e., a small oscillation of an already existing ground-state order, which can be triggered by a delicate but featureless excitation across the gap. Having generated the desired order, our aim is to stabilize the order even if the driving is switched off. Interacting systems undergo a synchronization transition where the order continues to show coherent oscillations. As a result, the generated space-time symmetry will then be imprinted on the electronic system, creating the possibility of stabilizing novel topologies and associated topological edge states. In short, we focus on the maintenance of the nontrivial order and the associated topological aspects that are caused by the dynamics in interacting electron system. We note that the synchronization transition that we find by our numerical approach turns out to be akin to the one discussed in the context of condensation of exciton and polariton [26,27]. In contrast to the discussions there, we show that a purely fermionic model with no coupling to bosons (e.g., photons) can still realize coherent oscillation.

The paper is organized in the following way: We consider irradiated graphene to generate the CDO using the periodic dynamics. Next, we treat the interaction using the mean field technique and explicitly write the mean field effective Floquet Hamiltonian in 2×2 form. We introduce another graphenelike model, containing an extra hopping term compared to graphene, that we use to check robustness of our findings in subsequent sections. Alongside, we also describe our method of numerical calculation. We discuss all the above topics in Sec. II. These Hamiltonians are derived and analyzed with further detail in Appendix A . After that, in Sec. III, we present our numerical findings and explain them with plausible arguments. In Sec. III A, we investigate the temporal dynamics of CDO and the impact of different parameters on the CDO oscillations. In Sec. III B, we examine the synchronization phenomena in graphene extensively. We define the synchronization order parameter that signals the dynamical synchronization transition (DST). We consider the other model to investigate the physics behind synchronization and its connection to the density of states more critically. Appendix B is devoted to the detail analysis of all the above findings. In order to motivate the experimental search, we analyze the behavior of current in Sec. III C. In Sec. III D, we study the emergence of space-time symmetry which leads to topological nature in the switch-OFF region. This is elaborately discussed in Appendix C with the dispersion of the edge states. For completeness, we incorporate the scattering effect in Sec. IV. The above section is further discussed in Appendix D. Finally, we conclude in Sec. V.

II. MODEL AND METHOD

In order to make the above argument solid, we use light-irradiated graphene [57] as an example since it is a prime test bed for theoretical and experimental researches [18,45–49]. We study electrons on the honeycomb lattice at half-filling described by the Hamiltonian

$$H = \frac{1}{N}\sum_{\boldsymbol{k}\sigma} \hat{\psi}^{\dagger}_{\boldsymbol{k}\sigma}\mathcal{H}(\boldsymbol{k}+\boldsymbol{A})\hat{\psi}_{\boldsymbol{k}\sigma},\, \mathcal{H}(\boldsymbol{k}) = \begin{pmatrix} 0 & h(\boldsymbol{k}) \\ h(\boldsymbol{k})^{*} & 0 \end{pmatrix} \quad (2)$$

with $\hat{\psi}^{\dagger}_{\boldsymbol{k}\sigma} = (c^{\dagger}_{A\boldsymbol{k}\sigma}, c^{\dagger}_{B\boldsymbol{k}\sigma})$ in the momentum $\boldsymbol{k}$ space, while A, B are the sublattice indices. The homogeneous electric field is introduced by a time-dependent gauge field $\boldsymbol{A}$. $h(\boldsymbol{k}) = \sum_{l=0}^{2} J e^{-i\boldsymbol{k}\cdot\boldsymbol{e}_l}$, $\boldsymbol{e}_l = (\cos\phi_l, \sin\phi_l)$ with $\phi_l = \pi/2 + 2\pi l/3$ sets the hopping and N is the number of unit cells in the lattice. The CDO and complex bond density order parameters are defined by

$$\Delta = \frac{1}{N}\sum_{\boldsymbol{k}} \Delta_{\boldsymbol{k}},\; b^{\pm} = \frac{1}{N}\sum_{\boldsymbol{k}} b^{\pm}_{\boldsymbol{k}} \quad (3)$$

with $\Delta_{\boldsymbol{k}} = \sum_{\sigma}\langle[c^{\dagger}_{A\boldsymbol{k}\sigma}c_{A\boldsymbol{k}\sigma} - c^{\dagger}_{B\boldsymbol{k}\sigma}c_{B\boldsymbol{k}\sigma}]\rangle$ and $b^{+(-)}_{\boldsymbol{k}} = \sum_{\sigma}\langle c^{\dagger}_{A(B)\boldsymbol{k}\sigma}c_{B(A)\boldsymbol{k}\sigma}\rangle$. How can we dynamically induce a CDO oscillation using laser? The order breaks the sublattice symmetry, reducing the lattice's C_{6v} crystalline symmetry down to C_{3v}. Bicircular laser, which is itself an experimentally well-established technique [58], can be expressed by a gauge field ($A = A_x + iA_y$)

$$A = A_L e^{i\omega t} + A_R e^{-2i\omega t + i\theta} \quad (4)$$

that also has this lower C_{3v} symmetry (we set $A_R = A_L$). This finally leads to the time-dependent two-level Hamiltonian

$$\mathcal{H}(\boldsymbol{k}+\boldsymbol{A}(t)) = \sum_{l=0}^{2}\begin{bmatrix} 0 & e^{i[k_x + A_x(t)]\cos\phi_l + i[k_y + A_y(t)]\sin\phi_l} \\ \text{H.c.} & 0 \end{bmatrix}, \quad (5)$$

where $A_x(t) = A_R\cos(\omega t) + A_L\cos(2\omega t - \theta)$ and $A_y(t) = A_R\sin(\omega t) - A_L\sin(2\omega t - \theta)$. Under the electric field $E(t) = -\partial_t A$, the A and B sublattices become inequivalent [Fig. 1(a)] and are expected to trigger the desired oscillation of Δ. A bicircular laser effectively induces terms that break the C_{6v} symmetry and the Floquet effective Hamiltonian includes an AB-sublattice potential $m_0\sum_{\boldsymbol{k}\sigma}[c^{\dagger}_{A\boldsymbol{k}\sigma}c_{A\boldsymbol{k}\sigma} - c^{\dagger}_{B\boldsymbol{k}\sigma}c_{B\boldsymbol{k}\sigma}]$. (This is detailed in Sec. II A, as well as in Appendix A 2.) This can push the electrons from A to B sublattices (or vice versa) initiating the oscillations.

Collective dynamics occur when we add electron-electron interactions

$$H_{\text{int}} = \frac{U}{2}\sum_{i} n_i n_i + V\sum_{\langle i,j\rangle} n_i n_j \quad (6)$$

to the free Hamiltonian (A2), where U and V denote the onsite and nearest-neighbor Coulomb repulsion, respectively ($n_i = \sum_{\sigma} c^{\dagger}_{i\sigma}c_{i\sigma}$, $\langle i, j\rangle$: nearest-neighbor pairs). The real-time dynamics of the extended Hubbard model at half-filling on the honeycomb lattice is studied within the time-dependent mean field approximation using

$$\mathcal{H}_{\text{MF}}(\boldsymbol{k}+\boldsymbol{A}) = \frac{1}{2}\begin{bmatrix} \left(\frac{U}{2} - 3V\right)\Delta & 0 \\ 0 & -\left(\frac{U}{2} - 3V\right)\Delta \end{bmatrix} + \mathcal{H}(\boldsymbol{k}+\boldsymbol{A}) + \left(\frac{U}{4} - \frac{3V}{2}\right)I \quad (7)$$

to govern the time evolution. Below, we set $J = 1$ to fix the energy scale and use $A_R = A_L = 1$. Since the combination $U/2 - 3V$(as denoted by $\lambda = U/2 - 3V$) is the only relevant interaction parameter within this approximation, we set $U = 0$ and use V as the parameter representing the correlation effect. Within the mean field approximation, the critical value for the ground-state CDO [59,60] transition is $V_c = 0.78$. In graphene [57], the material parameters are known to be close but below the critical value accommodating a semimetallic phase [61].

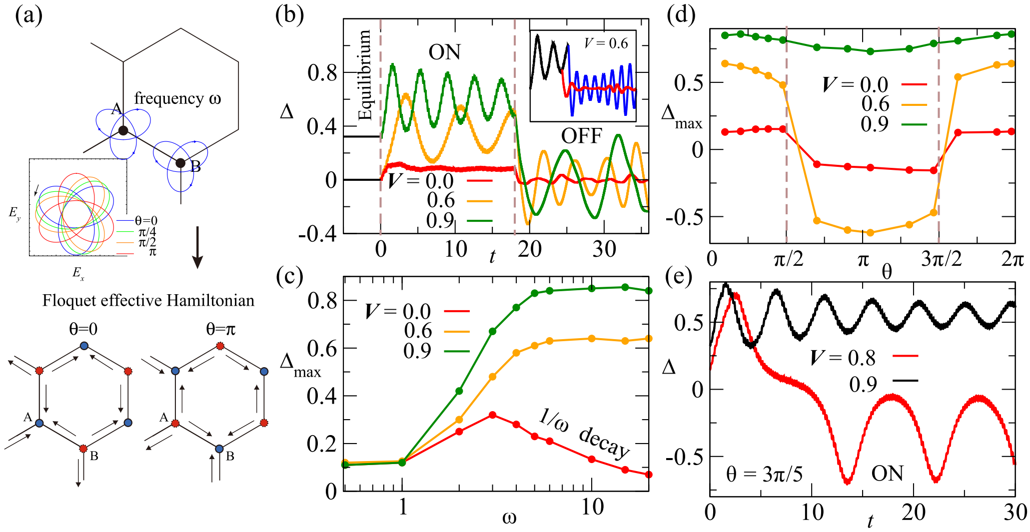

FIG. 1. (a) Bicircular laser field, as depicted by the blue curve, makes the A and B sublattices in the honeycomb lattice inequivalent (inset: angle dependence). When it is ON, effective terms such as an onsite AB-sublattice alternating potential is dynamically induced, which triggers a charge transfer (arrows). (b) Time evolution of the CDO parameter. The oscillation amplitude and the mean values of Δ are both enhanced by the interactions. Inset shows that for a given value of interaction strength ($V = 0.6$), the relaxation dynamics bears a prominent memory effect depending on the values of CDO particularly at the instance when laser field is switched OFF ($\omega = 10.5$, $\theta = \pi/10$). (c) The maximum value of the CDO $\Delta_{\max}$, during the bicircular driving, shows a significant increase in the interacting case for $\omega > 2$ ($\theta = \pi/10$). (d) The dependence of $\Delta_{\max}$ on the angle θ of the bicircular field. It switches sign around $\theta = \pi/2$ and $\theta = 3\pi/2$ ($\omega = 10.5$). (e) Starting within the CDO phase, it is possible to flip the order when we are near both the phase boundary and $\theta = \pi/2$.

A. Effective Hamiltonian in the switch-ON region

In this section, we briefly explain how the bicircular laser field results in the breaking of the AB-sublattice symmetry from the point of view of the Floquet effective Hamiltonian that governs the system in the switch-ON region. One can also obtain an effective Hamiltonian in switch-OFF region considering an oscillating CDO. For more technical details, we refer to Appendix A 2.

First, we elaborate the case when driving is present. One can consider the noninteracting limit with $V = U = 0$ and solve the problem in a time-independent approach using the Floquet theory. In order to write an explicit form of Brillouin-Wigner effective Hamiltonian H_{BW} one has to consider high-frequency limit $\omega \to \infty$. In the leading with respect to ω, H_{BW} in the real space is given by [62]

$$\begin{aligned}H_{\mathrm{BW}} = &\sum_{i,p}^{\mathrm{NN}} J_1 a_i^\dagger b_{i+p} + \sum_{i,p\neq q}^{\mathrm{NNN},A(B)} J_2^{A(B)} a(b)_i^\dagger a(b)_{i+p-q}\\ &+ \sum_{i,p\neq q\neq r}^{L\ \mathrm{links}} J_4 a_i^\dagger b_{i+p-q+r} + \sum_{i,p\neq q}^{M\ \mathrm{links}} J_3 a_i^\dagger b_{i+2p-q} + \mathrm{H.c.}\\ &+ \sum_{i}^{A(B)\ \mathrm{sublattice}} m_{A(B)} a(b)_i^\dagger a(b)_i + \mathrm{H.c.}\end{aligned} \quad (8)$$

Here, the fermion operators a_i (b_i) refer to the fermions on the $A(B)$ sublattices. J_1 and J_2 are the nearest-neighbor (NN) and next-nearest-neighbor (NNN) hopping while J_3 and J_4 are long-range hopping through different links on the lattice. $m_{A(B)}$ is the local mass term over $A(B)$ sublattice and satisfies $m_A = -m_B$ ($= m_0$). The interesting point to note here is that biharmonic driving generates higher-order hopping and onsite mass term. Therefore, we can argue that even without the interaction, CDO can be observed as long as the momentum-independent mass term breaks the inversion symmetry. Now, for the interacting case, we can not employ the Brillouin-Wigner expansion. But in the weakly interacting limit, the notion of effective Hamiltonian still exists. The generation of CDO as observed in Fig. 1(a) can be explained by the above Hamiltonian. We note that higher-order hopping is $O(\omega^{-2})$ and mass term is $O(\omega^{-1})$.

Moving back to momentum space, we can express Hamiltonian (8) in the weakly interacting limit as a two-level Hamiltonian in a generic way:

$$H_k(t) = \begin{bmatrix} \lambda\Delta(t) + m(t) & h_{\boldsymbol{k}} + h'_{\boldsymbol{k}} \\ h^*_{\boldsymbol{k}} + h'^*_{\boldsymbol{k}} & -\lambda\Delta(t) - m(t) \end{bmatrix}. \quad (9)$$

Here, the mass term $m(t)$ is induced effectively by the bicircular laser field and exists during the switch-ON region: $m(0 < t < t_f) = m_0$ and $m(t > t_f) = 0$, Here t_f is the time until which laser driving is on. We stress that there are many other terms in the effective Hamiltonian H_{BW} but this term plays the most dominant role in the charge order dynamics. The CDO parameter Δ appears like a mass term as we see it in Eq. (7). We emphasize that mass term is more stronger than higher-order sublattice hopping term in the high-frequency limit. Hence, modeling the problem with the mass term only would be more appropriate in the high-frequency limit (see Appendix A 2). The $h'_{\boldsymbol{k}}$ term represents higher-order hopping between A and B sublattices in (8) that is induced by the bicircular laser field and is present only in the switch-ON region. We can extend the notion of effective Hamiltonian in the switch-OFF region by considering an oscillating CDO

$\Delta(t)$ with $m(t) = 0$ and $h'_{\boldsymbol{k}} = 0$ (the detail discussion is given below in Sec. III D).

B. Numerical protocol

We here would like to mention a few technical details to calculate the CDO Δ in presence of interaction. We consider the momentum-space two-level graphene Hamiltonian (7) to carry out the time-dependent mean field treatment. We can determine $\Delta = \rho_A - \rho_B$ with $\rho_A = \sum_{\boldsymbol{k}} \langle c^\dagger_{A\boldsymbol{k}} c_{A\boldsymbol{k}} \rangle$ and $\rho_B = \sum_{\boldsymbol{k}} \langle c^\dagger_{B\boldsymbol{k}} c_{B\boldsymbol{k}} \rangle$ by directly diagonalizing the Hamiltonian given in Eq. (7).

Initial state preparation. Before going into dynamics, by an iterative method for a given value of U and V, we calculate Δ. In order to do this, we start from some random initial guess for ρ_A and ρ_B.

Time evolution. Once the ground-state CDO parameter Δ is determined, we proceed with time-dependent Schrödinger equation, governed by the Hamiltonian $\mathcal{H}_{\text{MF}}(\boldsymbol{k})$ [Eq. (7)] and solve it using the fourth-order Runge-Kutta method, while the order parameter $\Delta(t)$ is calculated at each time step. In the switch-OFF region, the same process continued without the explicit time dependence of the Hamiltonian, i.e., we continue the time evolution with Hamiltonian given in Eq. (7) with $A_x = A_y = 0$.

C. Effect of van Hove singularity: Introduction of model (ii)

We below find that the divergence of the density of states due to the van Hove singularity of the honeycomb lattice plays an important role in the synchronization dynamics (which we discuss in Sec. III B). In order to isolate this effect from the others, we introduce a lattice model, which we refer to as model (ii), by adding extra hopping terms to the pure honeycomb lattice [which we refer to as model (i)]. The Hamiltonian of model (ii) is given by adding a term $\delta\mathcal{H}(\boldsymbol{k}) = \sin(k_x - k_y)\cos(k_x + k_y)\sigma_x$ to the graphene Hamiltonian (2) and σ_x is the Pauli matrix.

III. RESULTS

We shall now discuss our main results in switch-ON and switch-OFF regimes in presence of interaction. First, we shall emphasize on the generation of CDO in the ON region and some interesting findings, e.g., flipping and memory effect associated with it. Then, in the OFF region, we show that a oscillating CDO order persists and we relate it to the synchronization between the momentum modes. We define a synchronization order parameter and relate it to the Kuramoto model. We also discuss the influence of density of states in these phenomena. We next extend our study to probe the dynamical synchronization transition by calculating an experimentally relevant quantity, e.g., current. Finally, our claim is that oscillatory CDO in the OFF region can lead to topological states that become long lived due to the presence of DST. This is a direction where one can play with space-time symmetries to generate a topological state even after the driving is OFF.

A. ON dynamics: CDO oscillation and flipping

We shall here present the results for switch-ON region. Figure 1(b) shows the time evolution of the CDO triggered by the bicircular pulse field (4). The field is suddenly ramped up and down at the beginning and end of the ON region. We checked that the findings qualitatively remain unaltered for slow ramping protocols.

Interactions substantially affect the CDO. They give rise to a pronounced oscillation both in the ON and OFF regions, where the amplitudes are controlled by the new energy scale set by V. Inset shows that even for the same interaction and pulse strength, the oscillation amplitude of Δ during the relaxation dynamics significantly depends on the value of Δ at which the field is switched off. This memory effect (or initial value effect) is completely absent for the noninteracting case. In Fig. 1(c), we further investigate ω and V dependence of Δ_{max}. The first observation is that CDO oscillations can be induced in a wide range of pump frequencies. However, a strong upturn occurs when $\omega = 2$ is exceeded. This is also where the interaction starts to assist the oscillation. For higher ω, we find that Δ_{max} saturates for the interacting case, in contrast to the noninteracting case, where Δ_{max} falls off as $1/\omega$, following high-frequency perturbation theory (see Appendix A 2). We note that the mass term m_0 in Eq. (9), mimicking the driving, is $O(1/\omega)$ for large ω.

The angle θ of the applied bicicular field plays a crucial role in controlling the CDO [see Fig. 1(d)]. For $\theta = 0,\ \pi$, it induces an effective AB-sublattice potential that favors a CDO, and Δ_{max} becomes largest with opposite signs as shown in Fig. 1(d). Flipping of already existing CDO is possible [see Fig. 1(e)]. We find that Δ can be flipped when we start in the ordered phase but not so far from the phase boundary. As for the direction of the bicircular field, the flipping started to occur above $\theta = \pi/2$ and became maximum around $3\pi/5$. Although we do not have a clear understanding of the flipping mechanism yet, at least in the noninteracting case, we find an analogous picture to the spin-echo (π-pulse) technique in NMR. Specifically, if we view the effective Floquet Hamiltonian (see Appendix A 2) as a spin Hamiltonian $\mu\mathbf{B}_{\boldsymbol{k}} \cdot \boldsymbol{\sigma}$, the order parameter Δ is analogous to a z-direction magnetization. We can connect the above spin Hamiltonian to Eq. (9) where the m_0 term also helps in building up the CDO. The situations for $\theta = 0, \pi$ correspond to having a z field since an effective AB-sublattice potential is induced and tries to align the spin in the z direction. However, once the order is established, a z-magnetic field that commutes with the order is not able to change it. On the other hand, the $\theta = \pi/2$ situation corresponds to having a transverse field, and it can be used to rotate the existing order Δ by suitably tuning σ_x and σ_y components in the effective Hamiltonian (see Appendix A 2). We can relate the $\sigma_{x,y}$ term of the above spin Hamiltonian as the higher-order hopping term $h'_{\boldsymbol{k}}$ [given in Eq. (9)] generated by the driving.

B. OFF dynamics: Synchronization order parameter

We now shall discuss our findings when the driving is OFF but the CDO oscillates. Density oscillations are usually quickly damped due to dephasing because electron-hole pair excitations, created by short and intense fields, spread out broadly in the energy-frequency space [63]. *Dynamical synchronization transition* (DST), ubiquitous in nonlinear dynamical systems, is a mechanism that acts against dephasing [64,65]. An ensemble of interacting oscillators with different frequencies can oscillate collectively at a single synchronization frequency Ω_0.

We make resort to the synchronization phenomena to explain the CDO oscillation. In the present system, the momentum-resolved CDO, current, and bond order parameters $[\{\Delta_{\boldsymbol{k}},\ J_{\boldsymbol{k}}=-i(b_{\boldsymbol{k}}^{+}-b_{\boldsymbol{k}}^{-}),\ K_{\boldsymbol{k}}=(b_{\boldsymbol{k}}^{+}+b_{\boldsymbol{k}}^{-})\}]$ define a three-dimensional vector field in the Brillouin zone. We find below that, while $K_{\boldsymbol{k}}$ changes only slowly, the $(\Delta_{\boldsymbol{k}}, J_{\boldsymbol{k}})$ component rotates around the $K_{\boldsymbol{k}}$ axis swiftly [with natural frequency $\Omega=2|h(\boldsymbol{k})|$ in the noninteracting case] and plays the role of the angle in the classical oscillator synchronization problem. The angle $\gamma_{\boldsymbol{k}}$ specifying the $(\Delta_{\boldsymbol{k}}, J_{\boldsymbol{k}})$ direction can be thought of as a generalized polarization direction. We can define [64,65] the collective phase ψ and amplitude r by

$$re^{i\psi}=\frac{1}{N}\sum_{\boldsymbol{k}} e^{i\gamma_{\boldsymbol{k}}},\quad e^{i\gamma_{\boldsymbol{k}}}=-\frac{\Delta_{\boldsymbol{k}}+iJ_{\boldsymbol{k}}}{|\Delta_{\boldsymbol{k}}+iJ_{\boldsymbol{k}}|}. \tag{10}$$

The amplitude $r\in[0,1]$ plays the role of the synchronization order parameter, and gives the fraction of the synchronized oscillators. For example, $r=1$ ($r=0$) means full (no) synchronization is achieved. A nonzero r signals a transition from a dephased state to a coherent one.

In the numerical simulation, we can obtain the synchronization order parameter as follows. We numerically compute the instantaneous wave function $(\psi_{\boldsymbol{k}}^{A}, \psi_{\boldsymbol{k}}^{B})$ solving the time-dependent Schrödinger equation with the Hamiltonian (7). We next compute the rotated wave function $u_{\boldsymbol{k}}(v_{\boldsymbol{k}})=1/\sqrt{2}[+(-)\exp(-i\phi_{\boldsymbol{k}}/2)\psi_{\boldsymbol{k}}^{A}+\exp(i\phi_{\boldsymbol{k}}/2)\psi_{\boldsymbol{k}}^{B}]$ to cast the Schrödinger equation in a special form where $\phi_{\boldsymbol{k}}=\mathrm{Arctan}[\mathrm{Im}(h_{\boldsymbol{k}})/\mathrm{Re}(h_{\boldsymbol{k}})]$. The polarization angle is then defined as $\gamma_{\boldsymbol{k}}=\gamma_{1,\boldsymbol{k}}-\gamma_{2,\boldsymbol{k}}$ with $\gamma_{1,2,\boldsymbol{k}}=\mathrm{Arctan}(\mathrm{Im}[u_{\boldsymbol{k}}(v_{\boldsymbol{k}})]/\mathrm{Re}[u_{\boldsymbol{k}}(v_{\boldsymbol{k}})])$. Now, one can calculate synchronization order parameter r as $r=\sqrt{(\sum_{\boldsymbol{k}}\sin\gamma_{\boldsymbol{k}})^2+(\sum_{\boldsymbol{k}}\cos\gamma_{\boldsymbol{k}})^2}/N$ and collective phase as $\psi=\mathrm{Arctan}(\sum_{\boldsymbol{k}}\sin\gamma_{\boldsymbol{k}}/\sum_{\boldsymbol{k}}\cos\gamma_{\boldsymbol{k}})$. The detail derivation is given in Appendix B 1.

We calculate the time evolution of the synchronization order parameter r for the two models [(i) i.e., graphene and (ii) i.e., graphene + extra hopping] as shown in Figs. 2(a) and 2(b), respectively. It has been observed that r oscillates around a finite value even the laser field is absent leading to fact that coherent dynamics continues irrespective of laser field. However, as expected, the magnitude of coherence or the degree of synchronization is higher in the switch-ON region. Another noticeable finding is that with the same strength of interaction $V=0.7$, r can behave differently in two different models.

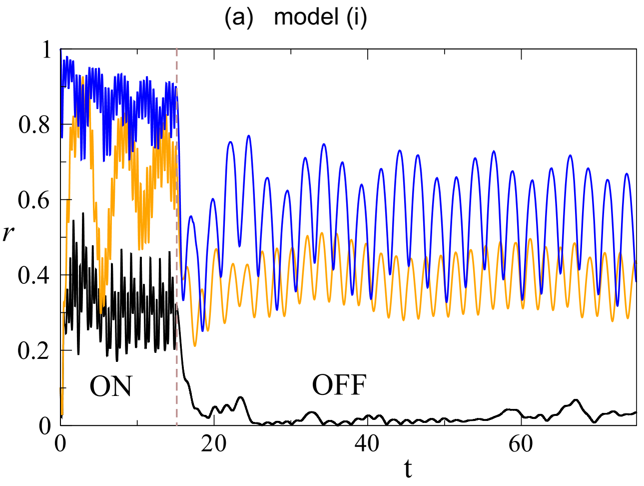
(a) model (i)

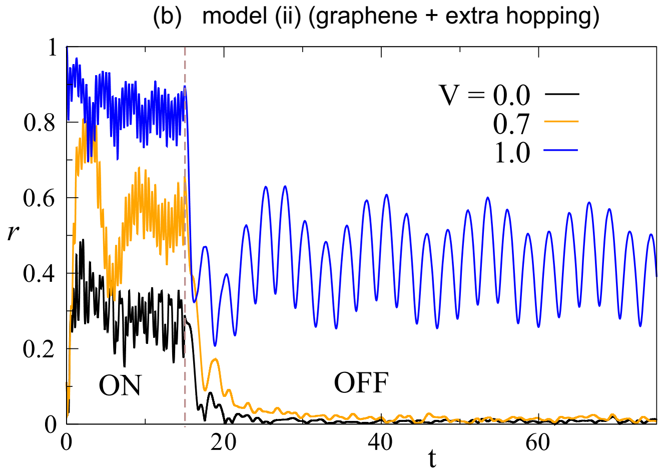
(b) model (ii) (graphene + extra hopping)

FIG. 2. (a) Time evolution of synchronization order parameter r for graphene [model (i)]. (b) Same as (a) for model (ii). We consider $\theta=\pi/10$ and $\omega=10$ and $N=100\times100$.

Direct evidence for DST can be obtained by evaluating the time-averaged value r_{av} as shown in Fig. 3(a), where we do the time average in the OFF region for a considerably long time span ($15<t<200$). As the interaction is increased, the synchronization order parameter increases monotonically, and we find a singular upturn associated with a nonanalytic behavior signifying a collective transition. This transition is dynamical in the sense that it depends on how the CDO is induced. For example, the critical interaction strength, referred as V_{DST}, depends on the details of driving, i.e., the frequency ω and field strength $A_L=A_R$ of the bicircular field as well as details of the underlying lattice model. An interesting observation is that r_{av} is nonzero even for the noninteracting case. This is due to the van Hove singularity in the density of states (DOS) at $\varepsilon_{\mathrm{vH}}=\pm1$ for the honeycomb lattice, representing a large fraction of coherent electron-hole pairs at $\Omega_0=2=2|\varepsilon_{\mathrm{vH}}|$. In order to isolate this effect, we study the DST by using a modified lattice Hamiltonian [model (ii)] with smoothened and broadened DOS without a singularity [see Fig. 3(b)]. There we find that r_{av} in the nonsynchronized phase stays at a smaller value approaching zero under a scaling analysis (as $N^{-1/2}$), and the transition becomes much more sharp and pronounced (see Appendix B 2).

We can obtain a deeper understanding of DST by looking into momentum-resolved synchronization correlation defined by ($t_i=15,\ t_f=50$)

$$S_{\boldsymbol{k}}=\frac{1}{\delta t}\int_{t_i}^{t_f}\Delta(t)\Delta_{\boldsymbol{k}}(t)dt \tag{11}$$

plotted in Figs. 3(c) and 3(d) for models (i) and (ii), respectively. We observe that the synchronization is taking place in the momentum space around the equal energy $[2|h(\boldsymbol{k})|=\mathrm{const}]$ contours close to the van Hove singularity in model (i) [blue dashed contour in Fig. 3(c)]. In model (ii), we see

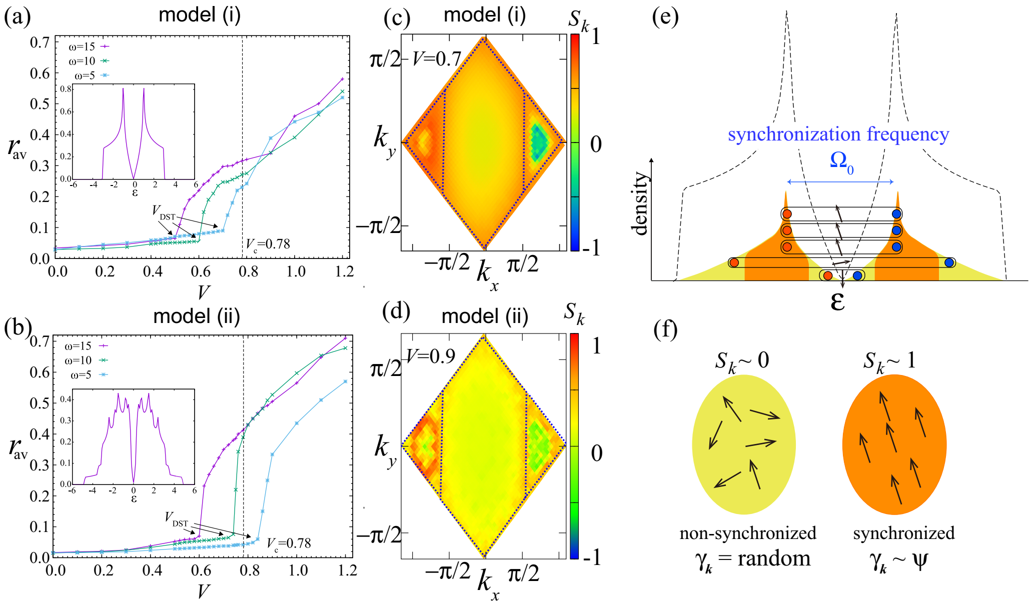

FIG. 3. (a) The synchronization order parameter (average value) $r_{\rm av}$ for the model on a honeycomb lattice ($\theta = \pi/10$, $N = 100 \times 100$). Inset shows the density of states. $V_{\rm DST}$ is the critical interaction strength for the DST to occur. (b) Same as (a) but with an altered lattice model [model (ii), see Appendix B 1] having a reduced singularity in its density of states. (c), (d) Momentum-resolved synchronization correlation $S_{\boldsymbol{k}}$ with $V = 0.7$ for model (i) and for model (ii) with $V = 0.9$, respectively ($\omega = 10$, $\theta = \pi/10$). Blue dotted line in (c) and (d) show the contour signifying the van Hove singularity [$|h(\boldsymbol{k})| = 1$], and the peak in the density of states, respectively. (e) Schematic plot of the electronic density of states (dashed) in the honeycomb lattice and the distribution of electron-hole pairs (solid). The latter is closely connected to $\int d^2\boldsymbol{k}|\Delta_{\boldsymbol{k}} + iJ_{\boldsymbol{k}}|\delta(\varepsilon - |h(\boldsymbol{k})|)$ and quantifies excitations due to pumping in the presence of interaction. The blue and red circles represent electron-hole pairs and the arrow refers to their polarization direction $\gamma_{\boldsymbol{k}}$. (f) Yellow and red regions schematically depict the nonsynchronized and synchronized states, respectively, in momentum (c), (d) and energy (e) spaces. The arrows illustrate $\gamma_{\boldsymbol{k}}$ and in the synchronized state, they rotate with a synchronization frequency Ω_0 and its direction defines the collective phase $\gamma_{\boldsymbol{k}} \sim \psi$.

qualitatively similar structure emerges from the now broadened peak of the density of states as shown in Fig. 3(d). The synchronization of the momentum modes can thus be depicted as the red region in Fig. 3(f) by rotors rotating with a common phase $\gamma_k \sim \psi$, while the yellow region illustrates the incoherent nonsynchronized case. Physically, the momentum-resolved order $(\Delta_{\boldsymbol{k}}, J_{\boldsymbol{k}})$ is associated to electron-hole pair excitation with energy $E_e - E_h \simeq 2|h(\boldsymbol{k})|$. Then, moving to the energy ε space, we can think of an intuitive picture as shown in Fig. 3(e). The pulse field excites electron-hole pairs with a broad distribution in energy space. Their polarization (designated by an arrow) starts to rotate individually with frequencies $\simeq 2|h(\boldsymbol{k})|$. Below the DST transition ($V < V_{\rm DST}$), they keep rotating incoherently and average out to zero. While above the DST ($V > V_{\rm DST}$), coherence among the electron-hole pairs is established collectively through interaction. The degree of synchronization is increased when the electron-hole pair density becomes higher. The synchronization frequency Ω_0 depends on the excitation distribution and its value is close to peak of the above distribution. Even in the synchronized state, there can be nonsynchronized excitations associated with energies away from $\hbar\Omega_0$.

What is the nature of the DST and how does the van Hove singularity affect it? Let us examine this by comparing models (i) and (ii) and their synchronization characteristics as plotted in Figs. 3(a), 3(c) and 3(b), 3(d). First, the nature of the transition around the transition point $V = V_{\rm DST}$ is qualitatively similar. The synchronization order parameter shows a singular upturn at $V = V_{\rm DST}$. In both cases, we found the same finite-size scaling $r_{\rm av} = a_0 + bN^{-1/2}$ (see the detail discussion in Appendix B 2) (N is the volume of the system) that is a characteristic of the Kuramoto model [65,66]. Thus, we infer that the DST in interacting electron systems treated at the mean field level is within the universal class of the Kuramoto model. Although it is not a necessary condition, the existence of the van Hove singularity surely assists the transition. This can be observed in the fact the the critical interaction $V_{\rm DST}$ is lowered in model (i) compared to model (ii) under the same conditions. Another effect is that when the density of states diverges, it leads to a trivial coherent oscillation making the value $r_{\rm av}$ to be finite even in the noninteracting case.

We shall now try to describe the phenomena of synchronization from the mathematical footing. We make resort to Kuramoto model to analyze the synchronization in the switch-OFF region. To be precise, the mathematical structure behind the DST can be elucidated as we relate the time evolution within the mean field approximation (7) to a variant of the Kuramoto model [64,65] that governs the dynamics of $\gamma_{\boldsymbol{k}}$ (see Appendix B 1). The time evolution of CDO and current order follow the time-evolution equation

$$\dot{\Delta}_k = -h_k J_k - \frac{2}{\Delta_k^2 + J^2}\left[\lambda \Delta_k J_k \sum_p \frac{\Delta_p}{N}\left(K_k + \frac{1}{K_k}\right)\right],$$

$$\dot{J}_k = h_k \Delta_k + \frac{2}{\Delta_k^2 + J^2}\left[\lambda \sum_p \frac{\Delta_p}{N}\left(K_k \Delta_k^2 - \frac{J_k^2}{K_k}\right)\right]. \quad (12)$$

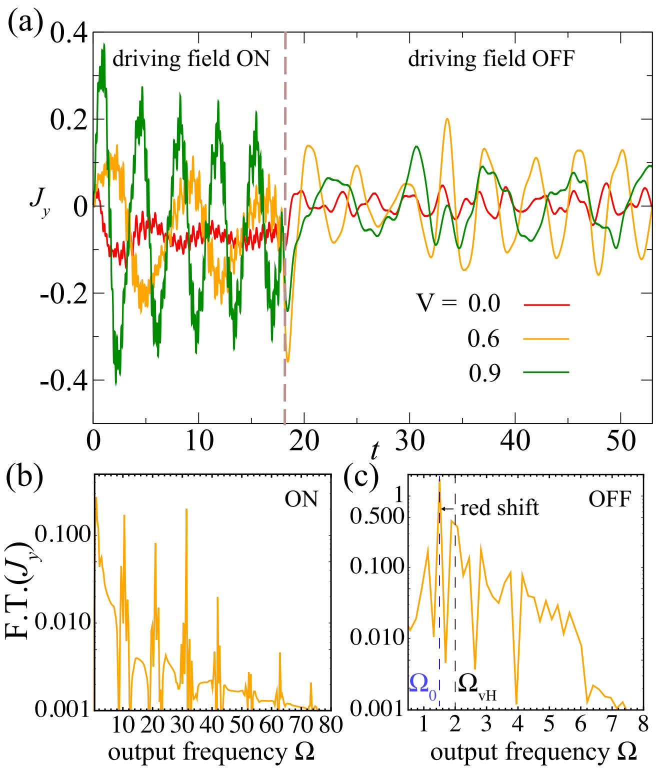

FIG. 4. (a) The time evolution of the current for the same parameters as Fig. 1(b). The Fourier transform of J_y in the (b) ON and (c) OFF regions. (b) Generation of higher harmonics is observed in the ON region. (c) In the OFF region, the synchronization frequency of the oscillation shows a redshift from the van Hove singularity ($\Omega_{\mathrm{vH}} = 2$) due to correlation effect to $\Omega_0 \simeq 1.5$. For (b) and (c), $V = 0.6$ is used, while $\theta = \pi/10$, $\omega = 10.5$ is used for all plots.

The mean field coupling can be mapped to the synchronization force associated with $\sum_p \Delta_p$ and the laser pumping to an external force associated with m_0. We note that $K_{\boldsymbol{k}}$ evolves slowly. The polarization angle $\gamma_{\boldsymbol{k}}$ is found to be $\gamma_{\boldsymbol{k}} = \mathrm{Arctan}(J_{\boldsymbol{k}}/\delta_{\boldsymbol{k}})$. Hence, $\gamma_{\boldsymbol{k}}$ bears the underlying connection between the different rotors via a mean field of interaction coupled to them. This framework is general and applies not only to graphene but to a wide variety of correlated electron systems even without the van Hove singularity and to their collective dynamics.

C. Experimentally measurable observable: Current

How can we experimentally verify the DST? While the CDO is not easily accessible, currents induced by a laser can be measured directly as shown by recent work on high harmonic generation (HHG) in graphene. Accordingly, we now investigate the nonequilibrium evolution of the induced current ($J_a = \sum_{\boldsymbol{k}\sigma} \psi^\dagger_{\boldsymbol{k}\sigma}[\partial\mathcal{H}(\boldsymbol{k}+\boldsymbol{A})/\partial k_a]\psi_{\boldsymbol{k}\sigma}$) as depicted in Fig. 4(a). The current shows a prominent beating pattern with increasing V in both ON and OFF regions. This beating reflects the CDO oscillation already presented in Fig. 1, as the current reflects the movement of charge between the A and B sublattices. Most interestingly, in the ON region, we observe the generation of higher harmonics, i.e., output frequency $\Omega = n\omega$ while investigating the Fourier component of the current [see Fig. 4(b)].

Concentrating on the OFF region, an oscillation with more prominent coherence in J_y is observed for V near V_c. A large peak at $\Omega_0 \sim 1.5$ is present in the Fourier spectrum of J_y [Fig. 4(c)]. The synchronization frequency Ω_0 is selected dynamically through a correlation effect and depends strongly on the electron-hole pair population density as we discussed after Fig. 3(e). The synchronization frequency Ω_0 is redshifted from the van Hove singularity $\Omega_{\mathrm{vH}} = 2$. This is because the electron-electron repulsion V, which is attractive between electrons and holes, reduces the pair energy from the bare value $2|h(\boldsymbol{k})|$ by its binding energy. There has been an optical luminescence experiment in graphene and the luminescence peak is found at 4.62 eV which is reduced from the expected bare van Hove energy 5.2 eV [67].

D. Road to self-maintained Floquet crystalline states

What is the consequence of having an oscillating mean field? An important point is that Floquet states are now self-maintained by the electronic degrees of freedom. They can remain even after the pump is finished as long as the oscillation exists. The Floquet state realized by DST has a crystalline symmetry now elevated to a space-time crystalline symmetry. For example, an oscillating CDO $\Delta = \Delta_0 \sin \Omega_0 t$ realizes a state with a time-glide symmetry. The mirror symmetry M for the mirror plane along the x axis between the AB sites is broken by Δ, but a time-glide symmetry $H(t, \mathbf{r}) = MH(t + T/2, \mathbf{r})M^{-1}$ ($T = 2\pi/\Omega_0$) is satisfied. To make this more specific, we considered the generation of such a naturally induced time-glide symmetry and its topological aspects in the Floquet condensation picture explicitly (see Appendix C). We consider the minimal model: $\mathcal{H}_{\boldsymbol{k}}(t) = \Delta(t)\sigma_z + h_x\sigma_x + h_y\sigma_y$ and $\Gamma = \sigma_z$; this model has a chiral symmetry $\Gamma\mathcal{H}_{\boldsymbol{k}}(t)\Gamma = -\mathcal{H}_{\boldsymbol{k}}(-t)$. In order to look for edge states, we consider an extra static magnetic field $B = (0, 0, B)$. This will modify the hopping through a phase factor $\exp(i\int A\,dr)$ with vector potential $A = (0, Bx, 0)$. Given this model, we consider an armchair edge in the brick-wall lattice geometry. We diagonalize the Floquet Hamiltonian (see Appendix A 1) to obtain the quasienergy, quasistates, and the associated average weight of each state on the lattice sites.

Indeed, by reverting to the minimal model introduced above, introduction of an oscillatory CDO term in the Hamiltonian can be shown to result in special edge states specific to Floquet states [22] for different parameter regimes. These edge states at the π gap in the quasienergy spectrum persist until the gap is closed and are related to the chiral symmetry of the system [68]. Nonetheless, while this is a particular example of a topological symmetry-protected state, this mechanism in general opens the door to access many new topological phases protected by new symmetries. Parallel to how the concept of topological insulators [32,33] is upgraded to topological crystalline insulators [69–73], the notion of Floquet topological insulators [18,19] can be refined by considering the space-time crystalline symmetry [74]. The DST, with the above example in particular, thus provides an experimentally viable route to realize long-lived Floquet topological crystalline insulators [75].

Another important point is the possibility of phason modes ϕ in Eq. (1). Windings can exist due to the equivalence $\phi(\boldsymbol{x}) \sim \phi(\boldsymbol{x}) + 2\pi$, leading to topological excitations. Examples include vortices and domain walls, which should bind nontrivial defect or edge modes similar to their static counterparts in Floquet topological crystalline insulators [76,77]. We will report on these issues elsewhere.

IV. BEYOND MEAN FIELD

Before closing, let us comment on the validity of our prediction which is based on the time-dependent mean field approximation. In real materials, relaxation due to phonons as well as electron-electron scattering processes is important. In particular, in graphene, it is known that phonon emission is the dominant relaxation channel, and the typical timescale for this to happen is a few hundred femtoseconds (fs) [78]. On the other hand, in our simulations, the unit of time is 1.8 fs considering the tunneling amplitude $J = 2.3$ eV for graphene. Thus, the synchronization oscillation period $T = 2\pi/\Omega_0 \simeq 8$ fs is well shorter than the relaxation timescale. As for electron-electron scattering process, considering the effect of a momentum-time-dependent random mass term that mimics scattering, we find that the coherence persists up to a certain realistic disorder strength (see Appendix D). Spontaneous emission is another source of relaxation, which is relevant for the physics of exciton polariton condensation [26,27]. However, this is very slow compared to the scattering processes and can be neglected in our treatment. We note that heating may take place in the ON region. However, our protocol uses short pulse excitation and we think that heating is not a severe problem in observing DST. This is because it is known that there exists a Floquet-prethermalization timescale below which the heating is negligibly small [79,80].

V. CONCLUSION

There exist a plethora of studies on Floquet topological insulators in the condensed matter community, but up to now, the exciting topological features have been limited in time by the duration of laser pulse. We introduced the concept of DST in a simple setup, where a tailored laser pulse is used to induce a collective electronic order dynamically. We find that DST paves the way to realize a Floquet topological state that is self-maintained and may become considerably long lived. In addition, DST gives a microscopic foundation to Floquet condensation, Eq. (1), as discussed in a holographic Floquet system [28]. Our findings also include general measurable features such as coherent light emission and HHG, as well as a realistic protocol to flip and control CDOs. Most importantly, our findings can be experimentally verified in real materials where relaxation due to phonons and electron-electron scattering processes is important as the synchronization oscillation period $T = 2\pi/\Omega_0 \simeq 8$ fs is well shorter than the experimentally observed relaxation timescales.

ACKNOWLEDGMENTS

We deeply thank A. Landsman for discussion on HHG in solids. T.N., T.O., and R.-J.S. acknowledge MPI-PKS for funding and support. T.O. also acknowledges MPI-CPfS for financial support.

APPENDIX A: FLOQUET DYNAMICAL SETUP

1. Quasienergy

Let us explain the Floquet quasienergy spectrum [18,19,37,81,82] of our model in the presence of bicircularly polarized laser field. The Floquet Hamiltonian acting on the Fourier components of the Floquet state takes the form

$$\mathbf{H} = \begin{pmatrix} \ddots & \vdots & \vdots & \vdots & \\ \cdots & \hat{H}_0 - \omega & \hat{H}_1 & & \\ & \hat{H}_{-1} & \hat{H}_0 & \hat{H}_1 & \\ & & \hat{H}_{-1} & \hat{H}_0 + \omega & \cdots \\ & \vdots & \vdots & \vdots & \ddots \end{pmatrix},$$

with $\hat{H}_n = \frac{1}{T}\int_0^T \mathcal{H}(\boldsymbol{k} + \boldsymbol{A}(t)) e^{it\omega n} dt$. Here, $\mathcal{H}(\boldsymbol{k} + \boldsymbol{A}(t))$ is the time-dependent lattice Hamiltonian as given in Eq. (2) of the main text:

$$\mathcal{H}(\boldsymbol{k} + \boldsymbol{A}(t)) = \sum_{l=0}^{2} \begin{bmatrix} 0 & e^{i[k_x + A_x(t)]\cos\phi_l + i[k_y + A_y(t)]\sin\phi_l} \\ \text{H.c.} & 0 \end{bmatrix}, \tag{A1}$$

where $A_x(t) = A_R \cos(\omega t) + A_L \cos(2\omega t - \theta)$ and $A_y(t) = A_R \sin(\omega t) - A_L \sin(2\omega t - \theta)$. Therefore, $\hat{H}_n$ is given by

$$\hat{H}_n = \begin{bmatrix} 0 & \sum_{l=0}^{2} t_{AB}^{n,l} e^{-i\boldsymbol{k}\cdot\boldsymbol{e}_l} \\ \sum_{l=0}^{2} t_{BA}^{n,l} e^{i\boldsymbol{k}\cdot\boldsymbol{e}_l} & 0 \end{bmatrix}, \tag{A2}$$

with $t_{AB}^{n,l} = \sum_m J_{-n-2m}(-A_R) J_m(A_L) e^{-im\theta} e^{\frac{i2\pi l(3m+n)}{3}}$ and the B-A hopping is given by $t_{BA}^{n,l} = \sum_m J_{-n-2m}(A_R) J_m(-A_L) e^{-im\theta} e^{\frac{i2\pi l(3m+n)}{3}}$.

We investigate the behavior of quasienergy as function of k_x with $k_y = 0$ as shown in Fig. 5. The gap at $\mathrm{K} = (K, 0)$ can be tuned by varying the frequency and amplitude. The gap at the other Dirac point $K' = (-K, 0)$ does not change significantly. The two quasienergies of two states residing in the same photon sector or in two consecutive time BZs come close for low amplitude and low frequency. The relative phase θ is able to tune both the gaps appearing at the Dirac points. The gaps at $(-K, 0)$ point change in an opposite way with θ. These points are identically gapped for $\theta = \pi/2$.

2. Brillouin-Wigner evaluation of the Floquet Hamiltonian

We now formulate the high-frequency effective Hamiltonian which enables us to study the phase diagram of Chern numbers in the various parameter space. To this end, we employ the Brillouin-Wigner (BW) perturbation theory to construct the high-frequency effective Hamiltonian on the projected zero-photon subspace of Floquet theory [62]. This correctly reproduces the quasienergies and the eigenstates associated with the original Floquet Hamiltonian up to order $1/\omega$. Specifically, a projector operator projects the whole Hilbert space $H \otimes T$ onto the zero-photon subspace $H \otimes T_0 \sim H$. On the other hand, the wave operator restores the eigenstates of $H \otimes T$ from the projected space of $H \otimes T_0$. The

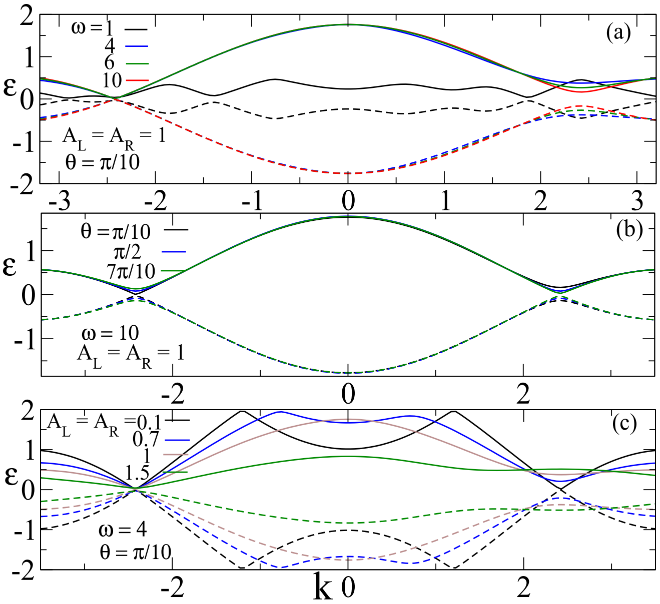

FIG. 5. Variation of quasienergy ε with k_x keeping $k_y = 0$ for different values of frequency (a), relative phase (b), and amplitude (c). (a) The gap at $(-K, 0)$ is much smaller than than of the at $(K, 0)$. This asymmetry of gaps is reduced as one increases ω, i.e., the gap appearing at $(K, 0)$ decreases, whereas, the other one changes insignificantly. The gap also increases in the central part with ω within the same temporal BZ. (b) Gap at $(-K, 0)$ increases with increasing θ within the range $0 < \theta < \pi$, while gap at $(K, 0)$ decreases. For $\theta = \pi/2$ both of them become symmetrically gapped. (c) Both the Dirac points are insignificantly gapped for smaller amplitude; the gap at $(K, 0)$ increases with A_L. Although, for smaller amplitude the gaps between two consecutive photon sectors appear symmetrically around $k_x = 0$, they disappear for higher amplitudes.

effective Hamiltonian is then expressed in terms of this wave operator that can be determined in powers of $1/\omega$ recursively. This theory has a number of advantages over the other high-frequency perturbation theories, namely, i.e., the Floquet-Magnus expansion and van Vleck expansion, being that the BW theory rectifies the driving phase dependence problem appearing in the Floquet-Magnus expansion. Additionally, BW theory can be used to get the higher-order terms which are challenging to compute using the van Vleck theory.

Having stated the BW theory in a nutshell, we revert to the associated final effective Hamiltonian $H_{\mathrm{BW}} = \sum_{n=0}^{\infty} H_{\mathrm{BW}}^{(n)}$ with

$$H_{\mathrm{BW}}^{(0)} = H_{0,0},\ H_{\mathrm{BW}}^{(1)} = \sum_{\{n_i\}\neq 0} \frac{H_{0,n_1} H_{n_1,0}}{n_1 \omega}$$

and

$$H_{\mathrm{BW}}^{(2)} = \sum_{\{n_i\}\neq 0} \left(\frac{H_{0,n_1} H_{n_1,n_2} H_{n_2,0}}{n_1 n_2 \omega^2} - \frac{H_{0,n_1} H_{n_1,0} H_{0,0}}{n_1^2 \omega^2} \right).$$

In the process of quantifying each term $H_{m,n}$ in the above expression, we need to compute the hopping strength accordingly in the presence of the laser fields [62]. The hopping strength from A sublattice to B sublattice becomes $t_{AB}^{n,l} = \sum_m J_{-n-2m}(-A_R) J_m(A_L) e^{-im\theta} e^{\frac{i2\pi l(3m+n)}{3}}$. Similarly, the B-A hopping is given by $t_{BA}^{n,l} = \sum_m J_{-n-2m}(A_R) J_m(-A_L) e^{-im\theta} e^{\frac{i2\pi l(3m+n)}{3}}$. While doing the calculation of the perturbation theory term by term, a variety of new hopping terms get generated. Below, we shall explicitly mention them.

We now explicitly write the NN hopping J_1 obtained from $H_{\mathrm{BW}}^{(0)}, H_{\mathrm{BW}}^{(2)}$ terms

$$a_i^\dagger b_{i+p} : J_1 = t_{AB}^{0,p} \tag{A3}$$

$$+ \sum_{n\neq 0} \frac{-1}{n^2\omega^2} \left(\sum_{q=0,1,2} t_{AB}^{-n,p} t_{BA}^{n,q} t_{AB}^{0,q} + \sum_{q=0,1,2}^{q\neq p} t_{AB}^{-n,q} t_{BA}^{n,q} t_{AB}^{0,p} \right)$$

$$+ \sum_{n,m\neq 0} \frac{1}{mn\omega^2} \left(\sum_{q=0,1,2} t_{AB}^{-n,p} t_{BA}^{n-m,q} t_{AB}^{m,q} \right)$$

$$+ \sum_{n,m\neq 0} \frac{1}{mn\omega^2} \left(\sum_{q=0,1,2}^{q\neq p} t_{AB}^{-n,q} t_{BA}^{n-m,q} t_{AB}^{m,p} \right), \tag{A4}$$

where p represents the links $l = 0, 1, 2$ for NN hopping. Now, NNN terms J_2, obtained from $H_{\mathrm{BW}}^{(1)}$, are given by

$$a_i^\dagger a_{i+p-q} : J_2^A = \sum_{n\neq 0} \frac{-1}{n\omega} t_{AB}^{-n,p} t_{BA}^{n,q}, \tag{A5}$$

$$b_i^\dagger b_{i+p-q} : J_2^B = \sum_{n\neq 0} \frac{-1}{n\omega} t_{BA}^{-n,p} t_{AB}^{n,q}. \tag{A6}$$

The mass terms m_A and m_B can be obtained from the above expressions of $a_i^\dagger a_{i+p-q}$ and $b_i^\dagger b_{i+p-q}$ with $p = q$. The third-nearest-neighbor hopping connected by M links [62] J_3, obtained from $H_{\mathrm{BW}}^{(2)}$, are given by

$$a_i^\dagger b_{i+2p-q} : J_3 = \sum_{n\neq 0} \frac{-1}{n^2\omega^2} \left[t_{AB}^{-n,p} t_{BA}^{n,q} t_{AB}^{0,p} \right]$$

$$+ \sum_{n,m\neq 0} \frac{1}{nm\omega^2} t_{AB}^{-n,p} t_{BA}^{n-m,q} t_{AB}^{m,p}, \tag{A7}$$

where $p \neq q = 0, 1, 2$. The other type of third-nearest-neighbor hopping connected by L links J_4 [62], obtained from $H_{\mathrm{BW}}^{(2)}$, is given by

$$a_i^\dagger b_{i+p-q+r} : J_4 = \sum_{n\neq 0} \frac{-1}{n^2\omega^2} \left[t_{AB}^{-n,p} t_{BA}^{n,q} t_{AB}^{0,r} \right]$$

$$+ \sum_{n,m\neq 0} \frac{1}{nm\omega^2} t_{AB}^{-n,p} t_{BA}^{n-m,q} t_{AB}^{m,r}, \tag{A8}$$

with $p \neq q \neq r = 0, 1, 2$. The Hermitian conjugate of the above terms [Eqs. (A4), (A7), and (A8)] gives the hopping from B sublattice to A sublattice; in this case, t_{AB} is replaced by t_{BA} and vice versa. The final Hamiltonian looks like

$$H_{\mathrm{BW}} = \sum_{i,p}^{\mathrm{NN}} J_1 a_i^\dagger b_{i+p} + \sum_{i,p\neq q}^{\mathrm{NNN},A(B)} J_2^{A(B)} a(b)_i^\dagger a(b)_{i+p-q}$$

$$+ \sum_{i,p\neq q\neq r}^{L \text{ links}} J_4 a_i^\dagger b_{i+p-q+r} + \sum_{i,p\neq q}^{M \text{ links}} J_3 a_i^\dagger b_{i+2p-q} + \mathrm{H.c.}$$

$$+ \sum_{i}^{A(B)\text{ sublattice}} m_{A(B)} a(b)_i^\dagger a(b)_i + \mathrm{H.c.} \tag{A9}$$

Hence, the high-frequency expansion gives rise to a momentum-independent mass term that breaks the inversion symmetry. We note that $m_A = -m_B = m_0$. This is the reason why CDO oscillates with real time inside the switch-OFF region. Having formulated the Hamiltonian in real space, one can go to Fourier space where $H_{\rm BW}$ is decomposed in different momentum segments, $H_{\rm BW} = \prod_k H_{\rm BW}^k$. The mass terms associated with σ_z are responsible for opening up a gap in the spectrum which eventually leads to nontrivial topological phases.

One can think of $H_{\rm BW}^k$ as a spin Hamiltonian with $\boldsymbol{k}$-dependent magnetic field terms, i.e., $H_{\rm BW}^k = \mu B_{\boldsymbol{k}} \cdot \sigma$. Since the 2×2, momentum-space effective Hamiltonian consists of the different kinds of hopping terms, e.g., nearest-neighbor hopping J_1, long-range hopping J_2, J_3, and J_4, and onsite terms $m_{A(B)}$. Among these terms, J_2 represents the hopping between the same sublattice. Therefore, the diagonal terms are given by momentum-independent mass terms along with the momentum dependent $J_2 \cos[\boldsymbol{k}(p-q)]$. On the other hand, the off-diagonal terms are given by $J_1 \exp(\pm i\boldsymbol{k}p)$, $J_3 \exp[\pm i\boldsymbol{k}(2p-q)]$, and $J_4 \exp[\pm i\boldsymbol{k}(p-q+r)]$. Therefore, the explicit momentum-dependent magnetic fields are $B_{\boldsymbol{k}x} = J_1 \cos(\boldsymbol{k}p) + J_3 \cos[\boldsymbol{k}(2p-q)] + J_4 \cos[\boldsymbol{k}(p-q+r)]$, $B_{\boldsymbol{k}y} = J_1 \sin(\boldsymbol{k}p) + J_3 \sin[\boldsymbol{k}(2p-q)] + J_4 \sin[\boldsymbol{k}(p-q+r)]$, $B_{\boldsymbol{k}z} = J_2 \cos[\boldsymbol{k}(p-q)] + (m_A - m_B)$. In order to clearly investigate the effect of each term, we study the momentum-independent coefficients, namely, J_1, J_2, J_3, J_4, and $m_A - m_B$ as a function of θ. This would provide a clear connection to the spin-echo analogy for $\theta = \pi/2$ as discussed in the main text.

Figure 6 shows the behavior of the effective terms while θ is varied. Since J_1 represents the nearest-neighbor hopping, its magnitude becomes largest among the hoppings. The M-link hopping refers to the maximum long-range hopping amplitude and hence its magnitude is the smallest, while L-link hopping is intermediate range. The interesting common fact about all the above hopping is that they all show oscillatory behavior with θ and acquire maximum magnitude at $\theta = \pi/2, 3\pi/2$. On the other hand, the NN-link hopping and L-link hopping both acquire minimum magnitude at $\theta = 0$. The M-links hopping becomes minimum for $\theta = \pi/4$, $3\pi/4$, $5\pi/4$, and $7\pi/4$. It again shows a secondary maxima at $\theta = 0$, π and 2π. On the other hand, for diagonal mass term $m_A - m_B$ changes its sign at $\theta = \pi/2$ and $3\pi/2$. It becomes maximally negative and positive at $\theta = 0$ and π. Therefore, it can be inferred that $\theta = 0$ and π refers to the two extreme situations where CDO acquires its maximum magnitude and the off-diagonal terms become insignificant. On the other hand, for $\theta = \pi/2$ and $3\pi/2$, the mass term becomes zero and gives room for the other terms to significantly alter the dynamics of the CDO.

Relating the above finding to the spin-echo technique, employed in NMR, one can say that z-component magnetization is caused by $B_{\boldsymbol{k}z}$. When the "transverse fields" $B_{\boldsymbol{k}x}$, $B_{\boldsymbol{k}y}$ acquire maximum values, the magnetization along the z direction can get flipped. This is due to the fact that $\sigma_{x,y}$ does not commute with σ_z and hence this off-diagonal term results in a precession. We note that the above argument is based on the Floquet effective Hamiltonian in the noninteracting case. For the interacting case, this argument is not guaranteed to hold. However, from our numerical findings, it still provides a qualitative understanding for the flipping of CDO as displayed in Fig. 1(e) (main text).

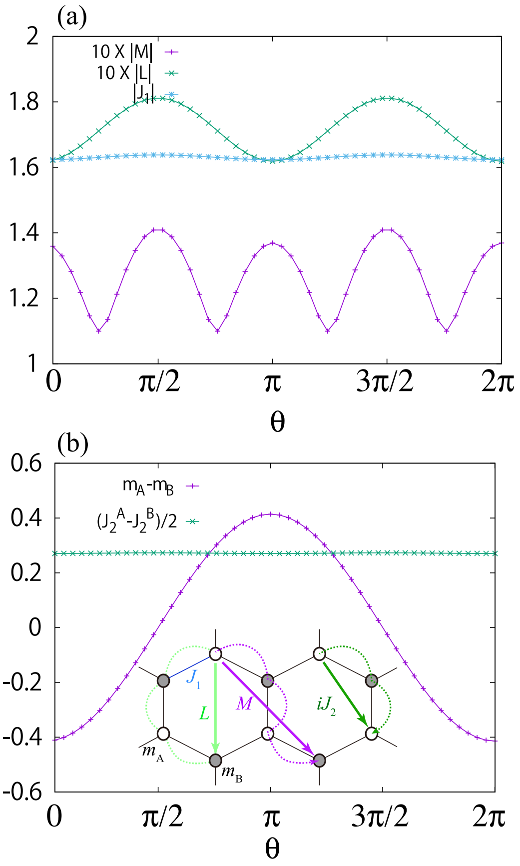

FIG. 6. (a) The plot shows the variation of the magnitude of the off-diagonal hopping terms with θ. As expected, $|J_1|$ is the most significant contributor and $|M|$ contributes insignificantly. The common fact is that $|J_1|$ and $|L|$ both exhibit a maxima near $\theta = \pi/2$ and a minima at $\theta = \pi$. While $|M|$ shows local maxima at $\theta = \pi/2$, π and minima at $\theta = 3\pi/4$. (b) The plot shows the diagonal mass terms and the hopping term to same sublattice as a function of θ. Interestingly, $m_A - m_B$ changes its sign when $\theta = \pi/2$. Inset depicts the geometrical description of different terms.

APPENDIX B: DYNAMICAL SYNCHRONIZATION TRANSITION

1. Time-dependent mean field approximation and a link to Kuramoto physics

Here, we outline the connection between the dynamics, based on the time-dependent mean field approximation, and the Kuramoto model, describing the synchronization transition for coupled pendulum. In order to simplify the argument, let us incorporate the effect of the bicircular laser field by an effective AB-sublattice alternating potential $m_A = m_0$, $m_B = -m_0$, which is justified using the high-frequency expansion. The model Hamiltonian then reads as

$$H_k(t) = \begin{bmatrix} \lambda\Delta(t) + m_0 & h_{\boldsymbol{k}} \\ h_{\boldsymbol{k}}^* & -\lambda\Delta(t) - m_0 \end{bmatrix} \tag{B1}$$

with the mean field potentials $\lambda\Delta(t)$ and $\Delta(t) \equiv \sum_{\boldsymbol{k}} \rho_{A,\boldsymbol{k}}(t) - \rho_{B,\boldsymbol{k}}(t)$, where $\lambda = (U/2 - 3V)$. Using unitary transformations $U_1 = \exp(-i\sigma_z\phi_k/2)$, $U_2 = \exp(-i\sigma_y\pi/4)$ with $\phi_k = \text{Arctan}[\text{Im}(h_k)/\text{Re}(h_k)]$, we reexpress the Hamiltonian in a more convenient rotated basis [83]

$$\hat{H}_k(t) = U_2U_1H_k(t)U_1^\dagger U_2^\dagger = \begin{bmatrix} |h_k| & \lambda\Delta(t)+m_0 \\ -\lambda\Delta(t)-m_0 & -|h_k| \end{bmatrix}. \tag{B2}$$

In this basis, the charge density order becomes $\Delta(t) = -2\sum_k \text{Re}(u_k^* v_k)$, where $u_k(v_k) = 1/\sqrt{2}[+(-)\exp(-i\phi/2)\,\psi_k^A + \exp(i\phi/2)\psi_k^B]$. The mean field equation of motion governing the dynamics can be written as follows:

$$i\dot{w}_k = 2|h_k|w_k + [\lambda\Delta(t)+m_0]\big(w_k^{-1} - w_k\big)w_k, \tag{B3}$$

where $w_k = u_k/v_k$.

Next, we rewrite this equation using the polarization angle γ_k using $u_k = \cos\theta_k \exp(i\gamma_{1,k})$ and $v_k = \sin\theta_k\exp(i\gamma_{2,k})$ under the condition of $|u_k|^2 + |v_k|^2 = 1$. This leads to $\Delta(t) = -\sum_p \sin(2\theta_p)\cos\gamma_p$, $\gamma_p = \gamma_{1,p} - \gamma_{2,p}$. One can readily show from Eq. (B3) that

$$\begin{aligned}
&\dot{\gamma}_k w_k - i\frac{2}{\sin(2\theta_k)}\dot{\theta}_k w_k \\
&\quad = 2|h_k|w_k - 2w_k\lambda\sum_p \sin(2\theta_p)\cot(2\theta_k)\cos\gamma_p\cos\gamma_k \\
&\qquad + 2iw_k\lambda\sum_p\frac{\sin(2\theta_p)}{\sin(2\theta_k)}\cos\gamma_p\sin\gamma_k \\
&\qquad + 2m_0w_k\bigg[-\cot(2\theta_k)\cos\gamma_k + i\frac{\sin\gamma_k}{\sin(2\theta_k)}\bigg].
\end{aligned} \tag{B4}$$

This further simplifies to two coupled first-order differential equations in θ_k and γ_k given by

$$\begin{aligned}
\dot{\gamma}_k &= 2|h_k| + 2\lambda\sum_p \sin(2\theta_p)\cot(2\theta_k)\times[\cos(\gamma_p-\gamma_k) \\
&\quad + \cos(\gamma_p+\gamma_k)] - 2m_0\cot(2\theta_k)\cos\gamma_k
\end{aligned} \tag{B5}$$

and

$$\dot{\theta}_k = \bigg(-m_0 + \lambda\sum_p\sin(2\theta_p)\cos\gamma_p\bigg)\sin\gamma_k. \tag{B6}$$

On the other hand, the generalized Kuramoto model [65,66,84–86] is represented by

$$\dot{\eta}_i = \omega_i + \sum_{j=1}^{N} M_{ij}\sin(\eta_i - \eta_j) + \epsilon_i(t) + F\sin(\sigma t - \eta_i) \tag{B7}$$

which governs the synchronization between N coupled (with coupling parameter M_{ij}) phase oscillators with phases η_i, oscillating with individual frequency ω_i. The F term represents the forcing strength. ϵ_i is a noise term that represents coupling to fast random degrees of freedom that leads to dissipation.

Comparing Eqs. (B5) and (B7), one can infer that γ_k plays the role of η_i in the Kuramoto model, and $2|h_k|$ of ω_i. From our numerical results, $\cos(\gamma_p+\gamma_k)$ in Eq. (B5) oscillates very fast and mimics the noise term ϵ_i. When the laser field is on ($m_0 \neq 0$), the last term of Eq. (B5) tries to pin the phases and, thus, corresponds to the forcing term in the Kuramoto model with $\sigma = 0$. The coupling M_{ij} is related to the $\lambda\sin(2\theta_p)\cot(2\theta_k)$ factor. This tells us two things. First, from the interaction dependence of the transition as shown in Fig. 2(a) in the main text, we notice that $\lambda[= (U/2 - 3V)]$ is the key resource for connecting different k modes leading to the DST. Second, the memory effect as shown in the inset of Fig. 1(b) (main text) can be understood by the $\sin(2\theta_p)\cot(2\theta_k)$ term. If we switch off the field when this term is small, the DST transition may not occur even when λ is sufficiently large.

The synchronization order parameter for the Kuramoto model defined by

$$r\,\exp(i\psi) = 1/N\sum_j\exp(i\eta_j) \tag{B8}$$

is evaluated numerically from our data in momentum space k by $r = \sqrt{(\sum_k\sin\gamma_k)^2 + (\sum_k\cos\gamma_k)^2}/N$ and $\psi = \text{Arctan}(\sum_k\sin\gamma_k/\sum_k\cos\gamma_k)$.

We note that the mean field equations (B5) and (B6) can also be expressed in terms of the momentum-resolved CDO Δ_k, current J_k, and bond order K_k parameters. The three-dimensional vector field in the momentum BZ is given by $\{\Delta_{\boldsymbol{k}}, J_{\boldsymbol{k}}, K_{\boldsymbol{k}}\} = \{-\sin 2\theta_{\boldsymbol{k}}\cos\gamma_{\boldsymbol{k}},\ -\sin 2\theta_{\boldsymbol{k}}\sin\gamma_{\boldsymbol{k}},\ \cos(2\theta_{\boldsymbol{k}})\}$. With the new variables $\tan\gamma_k = J_k/\Delta_k$, $\tan 2\theta_k = \sqrt{J_k^2+\Delta_k^2}/K_k$, 0 we can show (neglecting the $\dot{K}_k$ term since K_k evolves slowly) that the mean field equations can be recasted into

$$\begin{aligned}
\dot{\Delta}_k &= -h_kJ_k - \frac{2}{\Delta_k^2+J_k^2}\bigg[m_0J_k\bigg(K_kJ_k + \frac{\Delta_k}{K_k}\bigg) \\
&\quad + \lambda\Delta_kJ_k\sum_p\frac{\Delta_p}{N}\bigg(K_k + \frac{1}{K_k}\bigg)\bigg],
\end{aligned} \tag{B9}$$

$$\begin{aligned}
\dot{J}_k &= h_k\Delta_k + \frac{2}{\Delta_k^2+J_k^2}\bigg[\lambda\sum_p\frac{\Delta_p}{N}\bigg(K_k\Delta_k^2 - \frac{J_k^2}{K_k}\bigg) \\
&\quad - 2m_0J_k\bigg(\frac{J_k}{K_k} - K_k\Delta_k\bigg)\bigg].
\end{aligned} \tag{B10}$$

This expression highlights the interplay between current and CDO.

Moreover, we stipulate that in the weak interacting limit ($\lambda \ll 1$) our model may lead to chaos. This is because there are some literatures [87–89] studying the Kuramoto models that report the existence of the chaotic regime. We will report on this aspect elsewhere.

2. Investigating DST critically

Effect of the van Hove singularity. In order to investigate DST more clearly, we shall consider two lattice models : (i) graphene, and (ii) graphene with additional *AB* hopping terms, both in the honeycomb lattice geometry. The motivation behind considering this extra lattice model is to identify the influence of van Hove singularity in the DST. The additional off-diagonal hopping term $\sin(k_x - k_y)\cos(k_x + k_y)$ is able to reduce the van Hove singularity of the density of states as shown in the main text.

We study the time evolution for synchronization order parameter r for these above two models. The common findings observed in both the models are the following: Starting from the nonordered state ($V < V_c$), the order parameter r starts from zero because the phase is indefinite, and increases quickly as the field activates the oscillation in the ON region. r starts from unity if the ground state is ordered. Prominent interaction dependence shows up in the switch-OFF region. As the interaction is increased, the time-averaged synchronization order parameter increases monotonically. In the ON region, r stays at a higher value compared to that in the OFF region. This reflects the fact that driving enhances the degree of synchronization and this is again related to the generation of more electron-hole pairs during the driving. Now, the marked difference between them is that for $V = 0.7$, model (ii) with additional hopping does not show any trace of synchronization transition while model (i) already experiences the DST, i.e., r stays positive well above zero in the OFF region. Therefore, it is evident that the DST is not only depends on the external driving but also on the specific details of the model. The interesting point is that upon the inclusion of $\sin(kx - ky)\cos(kx + ky)(c^\dagger_{Ak\sigma}c_{Bk\sigma} + c^\dagger_{Bk\sigma}c_{Ak\sigma})$ term, the van Hove singularity is reduced and the density of states (DOS) gets smoothened and broadened. This has its impact on r in the switch-OFF region where r continues staying in much less values compared to model (i). This effect is clearly visible in Fig. 2 of the main text where $r_{\rm av}$ is plotted against V to show the DST in a more generic way. We use these data to calculate the average value of r, $r_{\rm av}$ as shown in Fig. 2 of the main text.

The striking difference between these two models is that the jump in $r_{\rm av}$ for model (ii) while undergoing a DST is much more than that of model (i). Therefore, the singularity in DOS yields some trivial synchronization even in the nonsynchronized phase where interaction is not able to initiate a collective phenomena. This results in a relatively high value of $r_{\rm av}$ in the above phase. While in the synchronized phase, the interaction plays the key role over the trivial synchronization factor. On the other hand, for model (ii), trivial synchronization is irrelevant and V plays the pivotal role. As a result, the difference between the values of $r_{\rm av}$ in synchronized and nonsynchronized phases is larger for model (ii) as compared to model (i). Consequently, a clear sharp and singular upturn is observed for model (ii) in Fig. 2(b) of the main text.

Scaling analysis. Having described the DOS dependence on $r_{\rm av}$, we shall now numerically try to establish the DST in a more concrete way by investigating the system size scaling properties of $r_{\rm av}$. We first check the behavior for larger system size in honeycomb graphene lattice model (i). For that, we set $V = 0.4$ in the nonsynchronized regime and $V = 0.9$ in the synchronized regime with $\omega = 10$. We obtain a power-law dependence of $r_{\rm av}$ on the system size

$$r_{\rm av} = a_0 + bN^{-1/2} \tag{B11}$$

in both the regimes (see Fig. 7). The $N^{-1/2}$ scaling is the same as the Kuramoto model [65,66]. Interestingly, the $N \to \infty$ value of $r_{\rm av}$, i.e., a_0 becomes very small [$O(10^{-2})$] for $V = 0.4$ as compared to $V = 0.9$. For the synchronized regime, $a_0 \simeq 0.26$, which now conveys that the synchronization transition is more clearly visible as we approach the thermodynamic limit. For validating our claim in a generic situation where the DOS is broadened and smoothened, we similarly investigate the model (ii). We find the same $N^{-1/2}$ scaling in both synchronized and nonsynchronized regimes with $a_0 \simeq 0.50$ and $O(10^{-2})$, respectively.

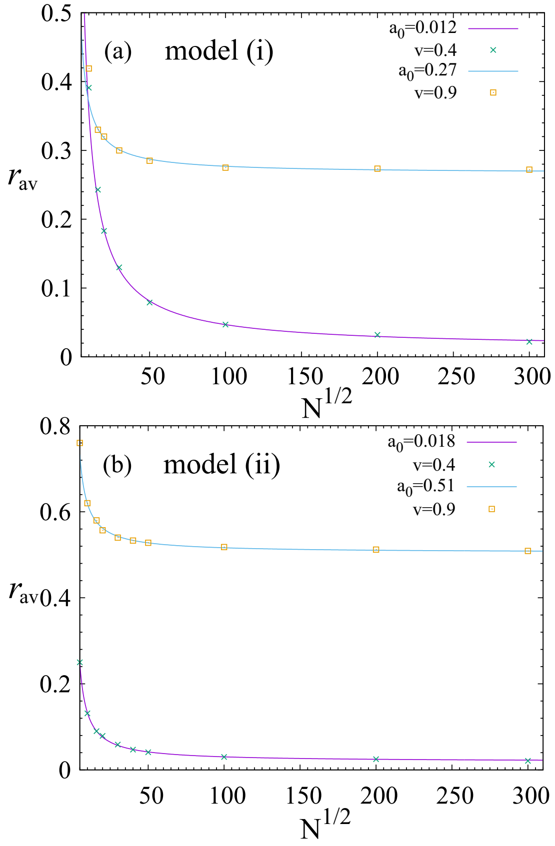

FIG. 7. (a) The plot shows that $r_{\rm av}$, obtained for model (i), follows a power-law scaling: $r_{\rm av} = a_0 + bN^{-1/2}$. Two distinct saturation values as captured by a_0 clearly suggest that there is synchronization transition. Plot (b) is the same as (a) but for the model (ii).

Synchronization correlation for model (ii). We further study the synchronization correlation $S_{\boldsymbol{k}}$ for model (ii) to investigate the location of synchronized region in the momentum space (see Fig. 8). For the noninteracting case, the rotors (i.e., $\gamma_{\boldsymbol{k}}$), rotating randomly, are not able to generate any synchronized motion from any part of the momentum space [see Fig. 8(a)]. This is in contrast to the case with model (i) where some momentum modes near the van Hove singularity actively participate in the synchronization leading to an enhancement in $r_{\rm av}$ even in the nonsynchronized phase. The interacting case with $V = 0.9$ for model (ii) is shown in Fig. 8(b). We find a strong synchronized region (red patch) around the left Dirac point K and in the energy space, this corresponds to the $\varepsilon \sim \pm 1.5$ line in DOS for model (ii) [as shown in the inset of Fig. 2(b) in the main text]. This refers to the fact that even when the singularity is absent, a peak in the density of states is enough to trigger the DST. We note that the K (left) and K' (right) points act differently in the $S_{\boldsymbol{k}}$ plot. This is because the bicircular laser field acts inequivalently to the two Dirac cones as explained in Appendix A 1.

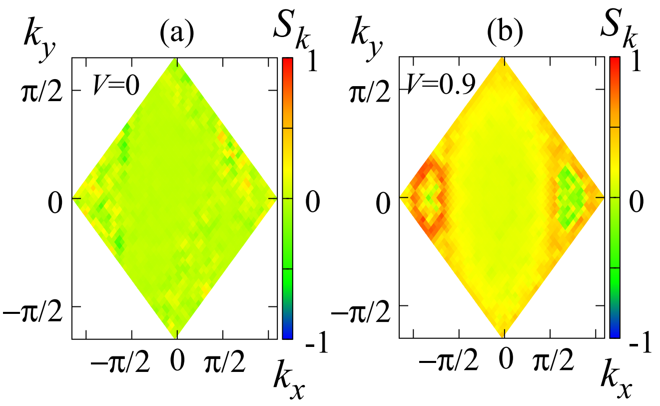

FIG. 8. The momentum-resolved density plot of S_k for model (ii) are shown in (a) with $V = 0$ and (b) with $V = 0.9$. The noninteracting case does not exhibit any sign of correlation in the whole BZ while for the interacting case, a strong correlation is built up close to equienergy surface enclosing Dirac point K.

APPENDIX C: TIME-GLIDE SYMMETRY, TOPOLOGY, AND ROAD TO SELF-MAINTAINED FLOQUET CRYSTALLINE STATES

We now investigate the emergence of edge state in a minimal model, considered for the switch-OFF region, with an open boundary condition in the x direction. Existence of such edge states that persist and appear upon band-gap closings, directly conveys the topological nature of the model in certain parameter regimes. This indicates the potential of DST setups to create novel Floquet crystalline states that are protected by space-time symmetries.

In the OFF region, when DST takes place, an oscillating CDO is formed. Let us investigate this situation using a simplified lattice model

$$H(t) = H_0 + \lambda\Delta(t)\sum_i (c^\dagger_{Ai}c_{Ai} - c^\dagger_{Bi}c_{Bi}), \tag{C1}$$

where H_0 denotes the noninteracting tight-binding model for electrons on the honeycomb lattice as given in Eq. (2) in the main text, and $\Delta(t) = m\,\sin(\Omega_0 t)$ represents the CDO oscillation and $\Omega_0 = 1.9$ is the system selected frequency. Importantly, this model has a chiral symmetry: $\Gamma\mathcal{H}_{\boldsymbol{k}}(t)\Gamma = -\mathcal{H}_{\boldsymbol{k}}(-t)$ in the momentum-space picture with $\mathcal{H}_{\boldsymbol{k}}(t) = \Delta(t)\sigma_z + h_x\sigma_x + h_y\sigma_y$ and $\Gamma = \sigma_z$. The corresponding real-space model has a time-glide symmetry as alluded in the main text, $H(t) = MH(t + T/2)M^{-1}$ ($T = 2\pi/\Omega_0$), where M is the mirror symmetry that is broken by the AB-sublattice potential. The Floquet topological crystalline states protected by the time-glide symmetry can now directly be investigated by checking whether the system supports π chiral edge states. Their existence is also closely tied to the chiral symmetry and has been proposed in theoretical models before [68]. In order to look for edge states, we consider an extra static magnetic field $B = (0, 0, B)$. This will modify the hopping through a phase factor $\exp(i\int A\,dr)$ with vector potential $A = (0, Bx, 0)$. Given this model, we consider an armchair edge in the brick-wall lattice geometry. We diagonalize the Floquet Hamiltonian to obtain the quasienergy, quasistates, and the associated average weight of each state on the lattice sites.

The results plotted in Fig. 9 show that, depending on the parameter regions, π edge modes indeed appear. The π edge modes are states spatially localized at the edge of the system appearing at $\varepsilon = \pm\Omega_0/2$ in the Floquet quasienergy space, and characterize dynamically extended topology of periodically driven systems [22]. We also find several topological transitions when the bulk gap vanishes and reopens. The left three panels of Fig. 9 convey that there is a topological transition between two topological phases as the field strength is increased as the gap closes and reopens at $B = 0.1$ while the strength of the CDO oscillation m is kept fixed to $m = 0.5$. We also remark that the topological phases are always characterized by an even number of edge modes, i.e., edge states appear always in pairs. For example, Fig. 9(a) depicts a situation where three pairs of modes appear at quasienergy $\varepsilon = \Omega_0/2$ at the left boundary and another three pairs of modes at the right boundary; each pair consists of two opposite chirality. Moreover, it is noteworthy that bulk bands close to $\varepsilon = \Omega_0/2$ become flat and the band gap vanishes at the topological transition point. One can also vary m to encounter a topological phase transition as observed in Fig. 9(e) with $B = 0.1$. In the right three panels of Fig. 9, we exemplify a situation where a topological phase is separated from a nontopological phase by a bulk gap closing. The nontopological phase does not contain any edge state at $\varepsilon = \Omega_0/2$. This asserts that topological phases protected by Floquet crystalline symmetries can indeed be induced by the DST setup.

APPENDIX D: BEYOND MEAN FIELD APPROXIMATION

We did not consider heating in our calculation. It has been a central topic of interest to study the heating effect in a periodically driven system. Recent studies in the context of many-body systems show that prethermalization takes place in the high-frequency regime [79,80,90]. What is argued there is that for a finite time window, the dynamics of an interacting system can be described within the Floquet effective Hamiltonian approach [90]. In our problem, the pulse duration of the laser field is finite and can be made short to fit within the Floquet prethermalization window.

We note that when the pulse duration becomes exponentially long, then the system would not be restricted inside the prethermal regime. Once the system starts absorbing energy, there would be substantial reduction of the synchronization. Hence, the synchronization order parameter r is expected to decrease. Similarly, in the switch-OFF regime, r would decrease. In order to clarify the heating effect arising from scattering, we perform an additional numerical calculation below.

In the mean field approximation, no scattering processes are considered. However, in order to accommodate the effect of relaxation due to electron-electron or electron-phonon scatterings, we extend the mean field treatment by considering a random mass term in the momentum space which changes its value for each momentum and time instant $M = \eta(t, k)$ with η chosen from a Gaussian distribution centered around zero. This term mimics the effect of a Hubbard-Stratonovich

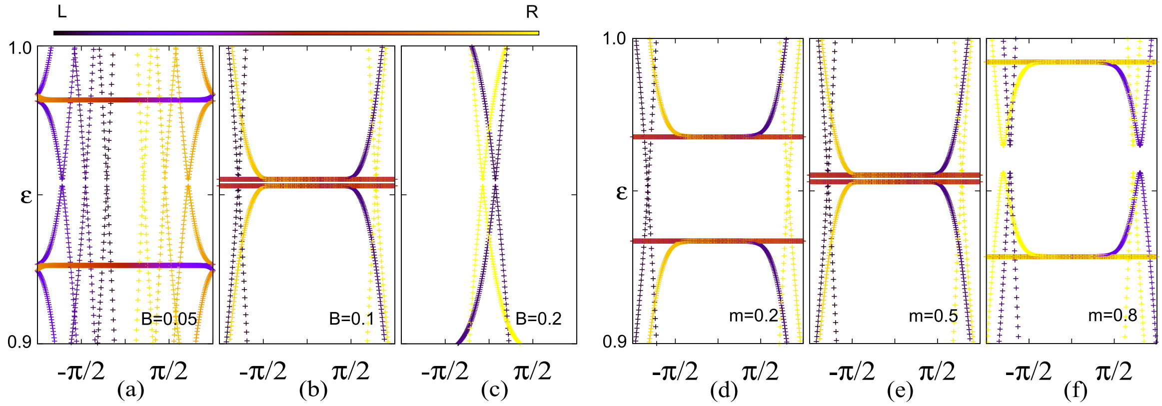

FIG. 9. Quasienergy dispersion of the Floquet Hamiltonian as function of k_y for various parameter values. The color map indicates the weight of states on each lattice site. The first three panels show that increasing B leads to a topological phase transition between two distinct topological phases by a closing of the bulk gap; here, m is kept at 0.5. (a) Topological phase with three pairs of edge states. (b) Closing of the bulk band gap due to the vanishing of the gaps between the flat bulk modes. (c) Another topological phase emerges with one pair of edge states. The last three panels show the transition from a topological phase to a nontopological phase by varying m keeping $B = 0.1$. (d) A situation where only one pair of edge states appear between the bulk flat band. (e) Bulk-gap closing. (f) Nontopological phase having no π edge states. In all cases, the lattice size $N = 200$.

field that arises when an electron-electron interaction is incorporated. The dynamical evolution of CDO Δ and the synchronization order parameter r are shown in Fig. 10. For low disorder strength, r is quantitatively unaltered in the both switch-OFF and -ON regions. The CDO behaves similarly as $M = 0$. For substantial disorder strength, r decreases in the switch-ON region. While in the switch-OFF region, r decreases to zero within a window of time after the switch-ON region. This window of time gradually decreases with increasing disorder strength. Therefore, the long time average

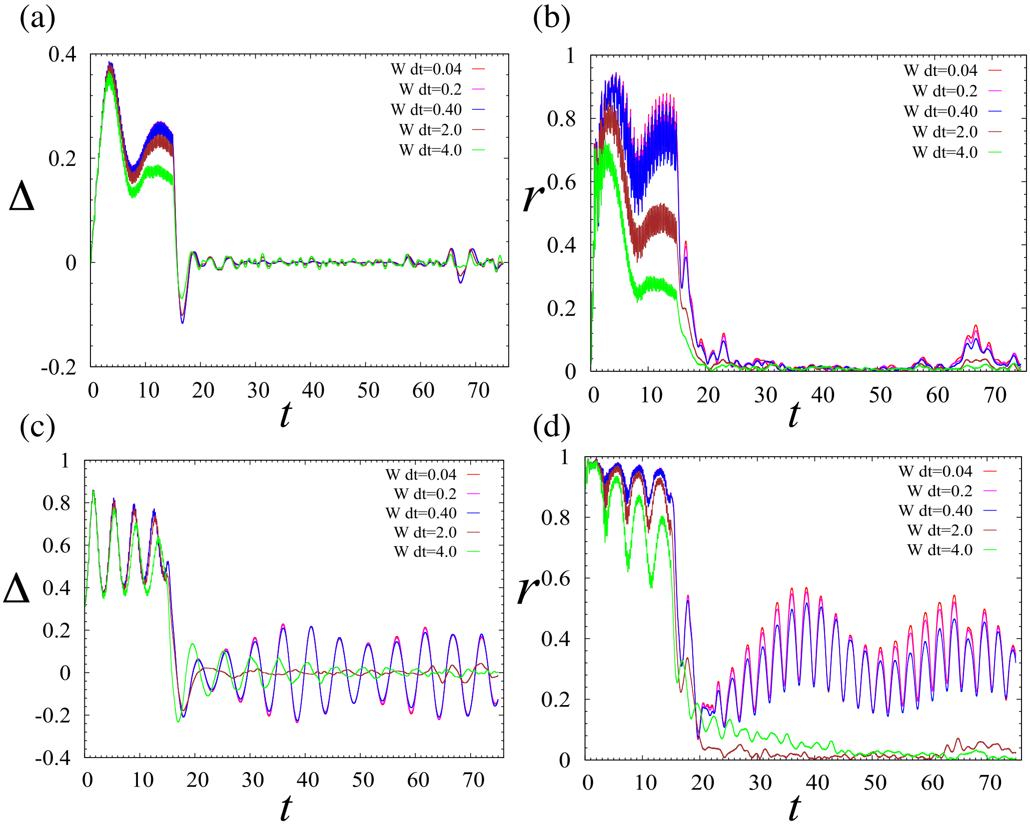

FIG. 10. The time evolutions of Δ and r are shown for $V = 0.3$ in (a) and (b), respectively. The same for $V = 0.8$ are shown in (c) and (d). Here, we consider graphene model (i) with momentum-time-dependent random mass term. The strength of this disorder is given by $W dt$. The synchronization is substantially affected by the disorder as observed for $V = 0.8$. Here, $\omega = 10$ and $\theta = \pi/10$.

value of r, $r_{\rm av}$ becomes zero when the disorder is substantial. This refers to the fact that the synchronization transition would disappear for strong disorder.

Now, we shall elaborate the above discussion The interesting observation in the OFF region is that for substantial disorder strength $W dt > 0.4$, CDO Δ continues to show coherent oscillation in a short window of time $15 < t < 40$ [see Fig. 10(c)]. Inside this temporal regime, r also remains finite, signifying the fact that the system remains in the synchronized phase [see Fig. 10(d)]. As time passes by $t > 40$, Δ starts dephasing and continues aperiodic random oscillation for further time. There, synchronization order parameter r decreases and becomes small. Hence, under a sufficiently long relaxation time, we expect that $r_{\rm av}$ as well as the oscillation amplitude in Δ diminish to zero. The time duration for which the coherence is remained is a few hundred time periods: $\delta t = 2m\pi/\omega$, with $m \sim O(10^2)$. The higher strength of the disorder is equivalent to a higher degree of momentum mixing due to the electron-electron scattering. For relatively small interaction strength $V = 0.3$, when graphene remains in a nonsynchronized phase with the same driving frequency, the temporal window δt becomes vanishingly small, as expected [see Figs. 10(a) and 10(b)]. Before closing, let us comment on the validity of our prediction which is based on the time-dependent mean field approximation.

We can now make some general comment regarding the scattering phenomena. We know from the existing literature that relaxation time in graphene is large compared to the strongly correlated cuprates where it is in femtoseconds. Experimentally, it has been shown that relaxation time in graphene is of the order of picoseconds or few hundred femtoseconds [78]. Additionally, in low temperature, the phonon scattering is reduced. On the other hand, in our simulations, the unit of time is 1.8 fs considering the tunneling amplitude $J = 2.3$ eV for graphene. Thus, the synchronization oscillation period $T = 2\pi/\Omega_0 \simeq 8$ fs is well shorter than the relaxation timescale. Hence, we think that even for real material in the presence of scattering and other relaxation mechanisms, a few cycles of coherent oscillation in Δ can be observed after switching off the laser field.

Numerical methods

We here would like to mention a few technical details to calculate the CDO in presence of interaction. We consider the momentum-space two-level graphene Hamiltonian (5) to carry out the time-dependent mean field treatment. First, we determine the initial value of ρ_A and ρ_B, before going into dynamics, by an iterative method for a given value of U and V; in order to do this, we consider some random initial guess for ρ_A and ρ_B. Once Δ is set in such a way, we proceed with time-dependent Schrödinger equation, governed by the Hamiltonian $\mathcal{H}_{\rm MF}(\boldsymbol{k})$ [Eq. (7)] and solved it again iteratively using the fourth-order Runge-Kutta method. In the switch-ON region with an explicit time-dependence Hamiltonian, we continue the iterative method replacing ρ_A and ρ_B at every step of time with their updated values as mean field results in a dynamical evolution of ρ_A and ρ_B. In the switch-OFF region, the same process continued without the explicit time dependence of the Hamiltonian.

[1] S. Iwai and H. Okamoto, J. Phys. Soc. Jpn. **75**, 011007 (2006).

[2] D. N. Basov, R. D. Averitt, D. van der Marel, M. Dressel, and K. Haule, Rev. Mod. Phys. **83**, 471 (2011).

[3] K. Yonemitsu and K. Nasu, Phys. Rep. **465**, 1 (2008).

[4] H. Aoki, N. Tsuji, M. Eckstein, M. Kollar, T. Oka, and P. Werner, Rev. Mod. Phys. **86**, 779 (2014).

[5] C. Giannetti, M. Capone, D. Fausti, M. Fabrizio, F. Parmigiani, and D. Mihailovic, Adv. Phys. **65**, 58 (2016).

[6] A. Cavalleri, C. Tóth, C. W. Siders, J. A. Squier, F. Ráksi, P. Forget, and J. C. Kieffer, Phys. Rev. Lett. **87**, 237401 (2001).

[7] S. Iwai, M. Ono, A. Maeda, H. Matsuzaki, H. Kishida, H. Okamoto, and Y. Tokura, Phys. Rev. Lett. **91**, 057401 (2003).

[8] L. Perfetti, P. A. Loukakos, M. Lisowski, U. Bovensiepen, H. Berger, S. Biermann, P. S. Cornaglia, A. Georges, and M. Wolf, Phys. Rev. Lett. **97**, 067402 (2006).

[9] S. Kaiser, C. R. Hunt, D. Nicoletti, W. Hu, I. Gierz, H. Y. Liu, M. Le Tacon, T. Loew, D. Haug, B. Keimer, and A. Cavalleri, Phys. Rev. B **89**, 184516 (2014).

[10] W. Hu, S. Kaiser, D. Nicoletti, C. R. Hunt, I. Gierz, M. C. Hoffmann, M. Le Tacon, T. Loew, B. Keimer, and A. Cavalleri, Nat. Mater. **13**, 705 (2014).

[11] R. Mankowsky, A. Subedi, M. Först, S. O. Mariager, M. Chollet, H. T. Lemke, J. S. Robinson, J. M. Glownia, M. P. Minitti, A. Frano, M. Fechner, N. A. Spaldin, T. Loew, B. Keimer, A. Georges, and A. Cavalleri, Nature (London) **516**, 71 (2014).

[12] T. F. Nova, A. Cartella, A. Cantaluppi, M. Först, D. Bossini, R. V. Mikhaylovskiy, A. V. Kimel, R. Merlin, and A. Cavalleri, Nat. Phys. **13**, 132 (2016).

[13] M. S. Foster, M. Dzero, V. Gurarie, and E. A. Yuzbashyan, Phys. Rev. B **88**, 104511 (2013).

[14] M. S. Foster, V. Gurarie, M. Dzero, and E. A. Yuzbashyan, Phys. Rev. Lett. **113**, 076403 (2014).

[15] N. Goldman, G. Juzeliūnas, P. Öhberg, and I. B. Spielman, Rep. Prog. Phys. **77**, 126401 (2014).

[16] A. Eckardt, Rev. Mod. Phys. **89**, 011004 (2017).

[17] T. Oka and S. Kitamura, Annu. Rev. Condens. Matter Phys. **10**, 387 (2019).

[18] T. Oka and H. Aoki, Phys. Rev. B **79**, 081406(R) (2009).

[19] N. H. Lindner, G. Refael, and V. Galitski, Nat. Phys. **7**, 490 (2011).

[20] T. Kitagawa, E. Berg, M. Rudner, and E. Demler, Phys. Rev. B **82**, 235114 (2010).

[21] L. Jiang, T. Kitagawa, J. Alicea, A. R. Akhmerov, D. Pekker, G. Refael, J. I. Cirac, E. Demler, M. D. Lukin, and P. Zoller, Phys. Rev. Lett. **106**, 220402 (2011).

[22] M. S. Rudner, N. H. Lindner, E. Berg, and M. Levin, Phys. Rev. X **3**, 031005 (2013).

[23] Y. H. Wang, H. Steinberg, P. Jarillo-Herrero, and N. Gedik, Science **342**, 453 (2013).

[24] G. Jotzu, M. Messer, R. Desbuquois, M. Lebrat, T. Uehlinger, D. Greif, and T. Esslinger, Nature (London) **515**, 237 (2014).

[25] M. C. Rechtsman, J. M. Zeuner, Y. Plotnik, Y. Lumer, D. Podolsky, F. Dreisow, S. Nolte, M. Segev, and A. Szameit, Nature (London) **496**, 196 (2013).
[26] N. Proukakis, D. Snoke, and P. Littlewood, *Universal Themes of Bose-Einstein Condensation* (Cambridge University Press, Cambridge, 2017).
[27] P. B. Littlewood and X. Zhu, Phys. Scr. T **68**, 56 (1996).
[28] S. Kinoshita, K. Murata, and T. Oka, J. High Energy Phys. 06 (2018) 096.
[29] K. von Klitzing, Rev. Mod. Phys. **58**, 519 (1986).
[30] D. C. Tsui, H. L. Stormer, and A. C. Gossard, Phys. Rev. Lett. **48**, 1559 (1982).
[31] D. J. Thouless, M. Kohmoto, M. P. Nightingale, and M. den Nijs, Phys. Rev. Lett. **49**, 405 (1982).
[32] X.-L. Qi and S.-C. Zhang, Rev. Mod. Phys. **83**, 1057 (2011).
[33] M. Z. Hasan and C. L. Kane, Rev. Mod. Phys. **82**, 3045 (2010).
[34] Y. Zhang, Y.-W. Tan, H. L. Stormer, and P. Kim, Nature (London) **438**, 201 (2005).
[35] X. Huang, L. Zhao, Y. Long, P. Wang, D. Chen, Z. Yang, H. Liang, M. Xue, H. Weng, Z. Fang, X. Dai, and G. Chen, Phys. Rev. X **5**, 031023 (2015).
[36] J.-i. Inoue and A. Tanaka, Phys. Rev. Lett. **105**, 017401 (2010).
[37] T. Kitagawa, T. Oka, A. Brataas, L. Fu, and E. Demler, Phys. Rev. B **84**, 235108 (2011).
[38] Z. Gu, H. A. Fertig, D. P. Arovas, and A. Auerbach, Phys. Rev. Lett. **107**, 216601 (2011).
[39] N. H. Lindner, D. L. Bergman, G. Refael, and V. Galitski, Phys. Rev. B **87**, 235131 (2013).
[40] E. Suárez Morell and L. E. F. Foa Torres, Phys. Rev. B **86**, 125449 (2012).
[41] Y. T. Katan and D. Podolsky, Phys. Rev. Lett. **110**, 016802 (2013).
[42] M. S. Rudner and L. S. Levitov, Phys. Rev. Lett. **102**, 065703 (2009).
[43] S. Diehl, E. Rico, M. A. Baranov, and P. Zoller, Nat. Phys. **7**, 971 (2011).
[44] T. Kitagawa, M. A. Broome, A. Fedrizzi, M. S. Rudner, E. Berg, I. Kassal, A. Aspuru-Guzik, E. Demler, and A. G. White, Nat. Commun. **3**, 882 (2012).
[45] P. Brumer and M. Shapiro, Chem. Phys. Lett. **126**, 541 (1986).
[46] K. L. Ishikawa, Phys. Rev. B **82**, 201402(R) (2010).
[47] J. Rioux, G. Burkard, and J. E. Sipe, Phys. Rev. B **83**, 195406 (2011).
[48] H. K. Kelardeh, V. Apalkov, and M. I. Stockman, Phys. Rev. B **91**, 045439 (2015).
[49] T. Higuchi, C. Heide, K. Ullmann, H. B. Weber, and P. Hommelhoff, Nature (London) **550**, 224 (2017).
[50] P. B. Littlewood and C. M. Varma, Phys. Rev. Lett. **47**, 811 (1981).
[51] P. B. Littlewood and C. M. Varma, Phys. Rev. B **26**, 4883 (1982).
[52] R. Matsunaga, K. Matsuda, and Y. Kanemitsu, Phys. Rev. Lett. **106**, 037404 (2011).
[53] R. Matsunaga, N. Tsuji, H. Fujita, A. Sugioka, K. Makise, Y. Uzawa, H. Terai, Z. Wang, H. Aoki, and R. Shimano, Science **345**, 1145 (2014).
[54] J. C. Tsang, J. J. E. Smith, and M. W. M Shafer, Phys. Rev. Lett. **37**, 1407 (1976).
[55] J. J. Demsar, K. Biljakovic, and D. Mihailovic, Phys. Rev. Lett. **83**, 800 (1999).
[56] D. Pekker and C. Varma, Annu. Rev. Condens. Matter Phys. **6**, 269 (2015).
[57] A. H. Castro Neto, F. Guinea, N. M. R. Peres, K. S. Novoselov, and A. K. Geim, Rev. Mod. Phys. **81**, 109 (2009).
[58] O. Kfir, P. Grychtol, E. Turgut, R. Knut, D. Zusin, D. Popmintchev, T. Popmintchev, H. Nembach, J. M. Shaw, A. Fleischer, H. Kapteyn, M. Murnane, and O. Cohen, Nat. Photonics **9**, 99 (2015).
[59] I. F. Herbut, Phys. Rev. Lett. **97**, 146401 (2006).
[60] S. Raghu, X.-L. Qi, C. Honerkamp, and S.-C. Zhang, Phys. Rev. Lett. **100**, 156401 (2008).
[61] T. O. Wehling, E. Şaşıoğlu, C. Friedrich, A. I. Lichtenstein, M. I. Katsnelson, and S. Blügel, Phys. Rev. Lett. **106**, 236805 (2011).
[62] T. Mikami, S. Kitamura, K. Yasuda, N. Tsuji, T. Oka, and H. Aoki, Phys. Rev. B **93**, 144307 (2016).
[63] T. Oka, Phys. Rev. B **86**, 075148 (2012).
[64] Y. Kuramoto, *Chemical Oscillations, Waves, and Turbulence* (Springer, Berlin, 1984).
[65] J. A. Acebrón, L. L. Bonilla, C. J. Pérez Vicente, F. Ritort, and R. Spigler, Rev. Mod. Phys. **77**, 137 (2005).
[66] F. A. Rodrigues, T. K. D. Peron, P. Ji, and J. Kurths, Phys. Rep. **610**, 1 (2016).
[67] K. F. Mak, J. Shan, and T. F. Heinz, Phys. Rev. Lett. **106**, 046401 (2011).
[68] T. Morimoto, H. C. Po, and A. Vishwanath, Phys. Rev. B **95**, 195155 (2017).
[69] L. Fu, Phys. Rev. Lett. **106**, 106802 (2011).
[70] R.-J. Slager, A. Mesaros, V. Juričić, and J. Zaanen, Nat. Phys. **9**, 98 (2012).
[71] J. Kruthoff, J. de Boer, J. van Wezel, C. L. Kane, and R.-J. Slager, Phys. Rev. X **7**, 041069 (2017).
[72] H. C. Po, A. Vishwanath, and H. Watanabe, Nat. Commun. **8**, 50 (2017).
[73] B. Bradlyn, L. Elcoro, J. Cano, M. G. Vergniory, Z. Wang, C. Felser, M. I. Aroyo, and B. A. Bernevig, Nature (London) **547**, 298 (2017).
[74] S. Xu and C. Wu, Phys. Rev. Lett. **120**, 096401 (2018).
[75] T. Nag, R.-J. Slager, T. Higuchi, and T. Oka (unpublished).
[76] R.-J. Slager, J. Phys. Chem. Solids **128**, 24 (2019).
[77] R.-J. Slager, A. Mesaros, V. Juričić, and J. Zaanen, Phys. Rev. B **90**, 241403(R) (2014).
[78] I. Gierz, J. C. Petersen, M. Mitrano, C. Cacho, I. C. E. Turcu, E. Springate, A. Stöhr, A. Köhler, U. Starke, and A. Cavalleri, Nat. Mater. **12**, 1119 (2013).
[79] D. A. Abanin, W. De Roeck, W. W. Ho, and F. Huveneers, Phys. Rev. B **95**, 014112 (2017).
[80] S. A. Weidinger and M. Knap, Sci. Rep. **7**, 45382 (2017).
[81] J. Shirley, Phys. Rev. **138**, B979 (1965).
[82] M. Griffoni and P. Hanggi, Phys. Rep. **304**, 229 (1998).
[83] R. A. Barankov, L. S. Levitov, and B. Z. Spivak, Phys. Rev. Lett. **93**, 160401 (2004).
[84] Y. Kuramoto, in *International Symposium on Mathematical Problems in Theoretical Physics*, edited by H. Araki (Springer, New York, 1975).

[85] Y. Kuramoto, *Chemical Oscillations, Waves and Turbulence* (Springer, New York, 1984).

[86] S. H. Strogatz, C. M. Marcus, R. M. Westervelt, and R. E. Mirollo, Phys. Rev. Lett. **61**, 2380 (1988).

[87] Y. Maistrenko, O. Popovych, O. Burylko, and P. A. Tass, Phys. Rev. Lett. **93**, 084102 (2004).

[88] V. Maistrenko, A. Vasylenko, Y. Maistrenko, and E. Mosekilde, Nonlin. Oscillations **11**, 229 (2008).

[89] L. M. Childs and S. H. Strogatz, Chaos **18**, 043128 (2008).

[90] T. Mori, T. Kuwahara, and K. Saito, Phys. Rev. Lett. **116**, 120401 (2016).